

A Late-Time View of the Progenitors of Five Type IIP Supernovae

Justyn R. Maund^{1,2,3*}, Emma Reilly¹ and Seppo Mattila⁴

¹ *Department of Physics and Astronomy, Queen's University, Belfast BT7 1NN, Northern Ireland, UK*

² *Dark Cosmology Centre, Niels Bohr Institute, University of Copenhagen, Juliane Maries Vej 30, 2100 Copenhagen, DK.*

³ *Royal Society Research Fellow*

⁴ *Finnish Centre for Astronomy with ESO (FINCA), University of Turku, Väisäläntie 20, FI-21500 Piikkiö, Finland*

7 November 2021

ABSTRACT

The acquisition of late-time imaging is an important step in the analysis of pre-explosion observations of the progenitors of supernovae. We present late-time HST ACS WFC observations of the sites of five Type IIP SNe: 1999ev, 2003gd, 2004A, 2005cs and 2006my. Observations were conducted using the *F435W*, *F555W* and *F814W* filters. We confirm the progenitor identifications for SNe 2003gd, 2004A and 2005cs, through their disappearance. We find that a source previously excluded as being the progenitor of SN 2006my has now disappeared. The late-time observations of the site of SN 1999ev cast significant doubt over the nature of the source previously identified as the progenitor in pre-explosion WFPC2 images. The use of image subtraction techniques yields improved precision over photometry conducted on just the pre-explosion images alone. In particular, we note the increased depth of detection limits derived on pre-explosion frames in conjunction with late-time images. We use SED fitting techniques to explore the effect of different reddening components towards the progenitors. For SNe 2003gd and 2005cs, the pre-explosion observations are sufficiently constraining that only limited amounts of dust (either interstellar or circumstellar) are permitted. Assuming only a Galactic reddening law, we determine the initial masses for the progenitors of SNe 2003gd, 2004A, 2005cs and 2006my of 8.4 ± 2.0 , 12.0 ± 2.1 , $9.5^{+3.4}_{-2.2}$ and $9.8 \pm 1.7 M_{\odot}$, respectively.

Key words: stars : evolution – supernovae : general – supernovae : individual : 1999ev – supernovae : individual : 2003gd – supernovae : individual : 2004A – supernovae : individual : 2005cs – supernovae : individual : 2006my

1 INTRODUCTION

All stars with initial masses $> 8 M_{\odot}$ are expected to end their lives as core-collapse supernovae (CCSNe). In the last decade, the direct observation of the progenitors of CCSNe in fortuitous pre-explosion imaging, has become an integral step in the study of all nearby events (for a review see Smartt 2009).

The majority of the success in the actual detection of progenitors has been for the Red Supergiant (RSG) precursors to hydrogen-rich Type II Plateau (IIP) SNe. The ensemble of progenitor detections and detection limits for these RSGs, however, presented a conflict with the theoretical expectation from stellar evolution models (Smartt et al. 2009). The ‘‘Red Supergiant Problem’’ refers to the apparent absence of progenitors of Type IIP SNe with mass $> 17 M_{\odot}$, whereas the theoretical expectation is that stars with masses up to $25 - 35 M_{\odot}$ should end their lives as RSGs. Recently Smith et al. (2011) and Walmswell & Eldridge (2012) considered the role of circumstellar dust, which is otherwise not probed by the resulting SN or the surrounding stellar population, as a possible so-

lution to the RSG problem. In particular, Walmswell & Eldridge established that the amount of circumstellar dust, and hence reddening, is larger for higher luminosity RSGs, that arise at the upper end of the mass range for stars to explode as Type IIP SNe. In the case of SN 2012aw, Fraser et al. (2012) and Van Dyk et al. (2012) observed a significant difference between the reddening determined towards the progenitor and the reddening inferred towards the subsequent SN; suggesting a significant amount of dust was associated with the progenitor and that it was destroyed in the SN explosion, such that it could not be measured post-explosion. Kochanek et al. (2012) and Van Dyk et al. (2012) also considered the additional possibility that the nature of the reddening, due to a circumstellar dust component, was different to ordinary reddening laws appropriate for the interstellar medium (e.g. Cardelli et al. 1989).

A further issue with the RSG problem is that the maximum mass is poorly constrained, due to the paucity of progenitors with high inferred masses. This may reflect either a real deficit of high mass progenitors (i.e. that the upper mass limit for stars to explode as Type IIP SNe is low) or may be due to low numbers of high mass progenitors according to the Initial Mass Function (IMF). The exact articulation and quantification of the RSG problem is compounded

* Email: j.maund@qub.ac.uk

by the reliance on, generally, poor fortuitous pre-explosion images, limited detections in pre-explosion images in multiple filters, and ambiguity as to whether the object observed at the SN position is indeed the progenitor object.

Maund & Smartt (2009) demonstrated that it is possible, using deep late-time images that are tailored (in a way that the pre-explosion images, by their fortuitous nature, cannot be) to observe the site of a given SN and overcome the severe limitations of analysis on just the pre-explosion images alone. Using image subtraction techniques, such as *isis* (Alard & Lupton 1998; Alard 2000), the late-time images can be used as templates, to both demonstrate the disappearance of the progenitor candidate (confirm the original identification) and conduct precise photometry (without contamination from nearby and underlying objects).

Here we present a new analysis of five previously identified progenitor candidates using newly acquired late-time HST Advance Camera for Surveys (ACS) Wide Field Channel (WFC) imaging. These progenitors are for SNe 1999ev, 2003gd, 2004A, 2005cs and 2006my, and details of these SNe are presented in Table 1.

2 OBSERVATIONS

The analysis of the pre-explosion HST observations of the sites of the five target SN progenitors has been previously presented by Maund & Smartt (2005) (1999ev); Van Dyk et al. (2003b), Smartt et al. (2004) and (Maund & Smartt 2009) (2003gd); Hendry et al. (2006) (2004A); Maund et al. (2005) and Li et al. (2006a) (2005cs); and Li et al. (2007), Leonard et al. (2008) and Crockett et al. (2011) (2006my). The pre- and post-explosion and late-time observations of the sites of the five target Type IIP SN progenitors are presented in Table 2.

2.1 Pre-explosion observations

Due to the availability of more recent and appropriate calibrations, new versions of the pre-explosion WFPC2 and ACS data were retrieved from the HST archive¹. The pre-explosion observations acquired with WFPC2 were drizzled together following the standard procedure². These images were produced for the purposes of image subtraction (see Section 2.6). In parallel, a separate “reduction” and photometric analysis was conducted on the same data using HST-phot (Dolphin 2000b). For SN 2005cs, pre-explosion images were acquired with the Advanced Camera for Surveys (ACS) Wide-Field Channel (WFC). These images were acquired using a four-point box dither pattern. Alignment between the images was checked using the PyRAF task *tweakshifts*, and the images were combined using *multidrizzle*. Due to the half-integer pixel shifts of the dither pattern it was possible to enhance the spatial sampling of the final image, providing a final pixel scale of 0.035". This is larger than exact half-sampling (0.025" px⁻¹), but is used to match the sampling achieved for the late-time ACS WFC images of SN2005cs (see Section 2.3).

2.2 Post-explosion observations

For the purposes of this study, the principal interest in the immediate post-explosion images (acquired up to 3 years post-explosion) was to provide a position for the SN relative to the surrounding stars, such that the SN position could be identified on the pre-explosion and late-time frames through differential astrometry. The “reduction” procedure for these images was the same as outlined for the pre-explosion observations (see Section 2.1).

2.3 Late-time ACS observations

Late-time observations of the sites of four of the target Type IIP SNe were acquired using the HST ACS WFC 1 for the program GO-11675 (PI Maund). The WFC chip was windowed to an array of 1k × 1k pixels to reduce the readout time and mitigate the role of Charge Transfer Inefficiency (CTI). Observations were conducted in three filters *F435W*, *F555W* and *F814W*. Importantly, for two SNe (2003gd and 2004A) the use of the *F555W* filter in these late-time observations *does not* match the pre-explosion images acquired with the wider *F606W* filter. In the pre-explosion frames, the majority of the flux from the progenitor at these wavelengths is representative of the continuum (requiring a small *F555W* – *F606W* colour correction). At late-times, however, the *F606W* filter encompasses the wavelength of *H α* , which is a characteristic emission feature of late-time Type IIP SN spectra. A more appropriate comparison between before and after continuum fluxes is, therefore, achieved with the *F555W* filter although, as discussed below, corrections for the slightly different filter transmission functions also need to be considered. Each of these late-time observations is composed of four separate sub-exposures acquired in a 4-point box dither pattern. This arrangement was used to permit the acquisition of better spatial sampling of the point-spread function (PSF) and for removal of fixed hot-pixel features. The PyRAF task *multidrizzle* was used to drizzle each of the sub-exposures (for a given filter) together. The task *tweakshifts* was used to fine-tune the alignment between each of the sub-exposures prior to drizzling. Although the 4-point box dither pattern employs half-integer pixel shifts, potentially giving an improvement of spatial sampling by a factor of 2, the presence of aliasing (alternating bands across the frames) prohibited reaching this final pixel-scale. This phenomenon was relatively insensitive to the choice of the drizzling kernel. Instead the final pixel scale is greater than one half of the original 0.05" pixel scales of ACS/WFC (0.035" px⁻¹).

For SN 2006my, observed for program GO-12282 (P.I. D. Leonard), the late-time images were only acquired in two bands (*F555W* and *F814W*). For each filter, two exposures were acquired, for the rejection of cosmic rays, but at the same pointing such that no spatial resampling was possible. These images for each filter were combined using *multidrizzle*, but with the output images having the original ACS/WFC pixel scale (0.05" px⁻¹).

2.4 Geometric Transformations

A series of transformations were calculated for the complete datasets to determine the positions for objects in a common reference frame. Geometric transformations were calculated between the pre-, post-explosion and late-time *F555W* images (or, if unavailable, *F814W* images) using the IRAF task *geomap*, assuming only simple offsets, rotations and scalings. For the data at a given epoch, shifts between images with other filters and the corresponding reference *F555W* image were calculated by cross-correlating

¹ <http://archive.stsci.edu>

² http://www.stsci.edu/hst/wfpc2/analysis/WFPC2_drizzle.html

Table 1. Details of the five target Type II SNe, with progenitor candidates identified in pre-explosion HST images.

Supernova	Type	Host Galaxy	Distance ¹ (Mpc)	$E(B - V)_{gal}^2$	$[O/H]^3$ (dex)
1999ev	II(P)	NGC 4274	15.1 ± 2.6	0.020	8.5
2003gd	IIP	NGC 628 (M74)	9.3 ± 1.8	0.061	8.4
2004A	IIP	NGC 6207	20.3 ± 3.4	0.014	8.3
2005cs	IIP	NGC 5194 (M51)	8.4 ± 1.0	0.031	8.7
2006my	IIP	NGC 4651	22.3 ± 2.6	0.024	8.7

¹ After Smartt et al. (2009).² After Schlafly & Finkbeiner (2011), as quoted by NED.³ Smartt et al. (2009).

these images with the *F555W* image as the reference frame. The cross-correlation was facilitated using the PyRAF task *crosscor*, with the corresponding shifts calculated using *shifffind*.

2.5 Photometry

For WFPC2 pre-explosion images the HSTphot package (Dolphin 2000b) was utilised to conduct PSF-fitting photometry of the input images. HSTphot provides the appropriate corrections for aperture size and charge transfer inefficiency, as well as tools for conducting artificial star tests. We note that HSTphot only provides aperture corrections to a final aperture size of $0.5''$. Using the corrections of Holtzman et al. (1995), we apply a term to correct to the photometry to an infinite aperture.

For data acquired for program GO-11675 (PI Maund), principal photometry was conducted using IRAF DAOPHOT on the final output drizzled images with the enhanced spatial sampling. We used the latest zeropoints appropriate for ACS WFC³. Aperture corrections were calculated for each image to an aperture of $0.5''$, with a further correction to infinity adopted from Sirianni et al. (2005).

A key concern for the fidelity of the derived photometry is the inefficiency of charge transfer (CTI) for charged coupled detectors on HST. As photometry was conducted on the drizzled, subsampled images, evaluating the magnitude of the CTI on the final photometry is non-trivial and is based on the position of a given star on the original undrizzled, distorted *FLT* images. Geometric transformations were calculated between the final drizzled images and the *FLT* images, using 3rd order polynomials in x and y , using *geomap*. This approach was used, over using a simple pre-computed distortion table, as non-negligible shifts were found between the expected pointings in the dither pattern. The positions of stars on the output drizzled images were transformed to the corresponding locations on each of the four constituent *FLT* images. Following Annibali et al. (2008), we conducted small aperture (3px) photometry on the individual *FLT* images and used the measured flux and sky background values to calculate the magnitude loss due to CTI following the analytic prescription of Chiaberge et al. (2009). Prior to conducting aperture photometry, the *FLT* images were scaled with the corresponding Pixel Area Map⁴. For a given star it might be only possible to calculate the magnitude loss for 1 or 2 of the input *FLT* images, because of the relative positions of bad pixels or cosmic rays. An average CTI loss (as a magnitude) was determined over the four constituent *FLT* images and applied to the photometry derived from the drizzled images.

In addition, photometry of the ACS images was also conducted using the DOLPHOT package⁵. We utilised two implementations of DOLPHOT for photometry of the ACS data: DOLPHOT with the ACS module on the distorted *CRJ* and *FLT* frames (which we refer to as DOLPHOT/ACS) and DOLPHOT as a generic photometry package for the distortion-corrected drizzled frames. We find excellent agreement between our DAOPHOT photometry and the photometry derived using HSTphot and DOLPHOT, within the limits of the photometric uncertainties. Similarly to HSTphot, the ACS photometry was corrected from a $0.5''$ to an infinite aperture, using the corrections tabulated by Sirianni et al. (2005)

The data for SN 2006my were analysed separately using only the HSTphot and DOLPHOT packages for the WFPC2 and ACS data, respectively.

2.6 Image Subtraction

Image subtraction techniques were used to conduct template subtraction of the late-time images from the pre-explosion images to: 1) confirm the identities of the progenitors through disappearance; and 2) conduct optimal differential photometry, independently of the background, of the now absent progenitors. We utilised the ISIS v2.2 image subtraction package (Alard & Lupton 1998; Alard 2000), which matches the PSFs of the input and template/reference images (as well as refining the alignment between the two images and scaling the flux levels). In addition, ISIS also provides automatic object detection and photometry on the difference images. We also tested our image subtractions using the HOTPANTS image subtraction package⁶, and examined the resulting difference images using DAOPHOT. We found no systematic difference between the photometry of difference images calculated using the two packages, and for this study use photometry derived from difference images constructed using ISIS

For each SN the late-time images were, generally, used as the reference images. The late-time images were transformed to match the pre-explosion images using IRAF task *geotran*. This ensured that we avoided resampling the lower quality pre-explosion images to match the superior late-time images.

The evaluation of the systematic uncertainties was conducted by varying the key parameters in ISIS that principally affected the output photometry: the number and size of the stamps used for calculating the kernel, the degree of the kernel variation across the field and the degree of the background fitting function. A major

³ <http://www.stsci.edu/hst/acs/analysis/zeropoints/#tablestart>⁴ <http://www.stsci.edu/hst/acs/analysis/PAMS>⁵ <http://americano.dolphinim.com/dolphot/>⁶ <http://www.astro.washington.edu/users/becker/hotpants.html>

Table 2. HST observations of the sites of the five target Type II SNe.

	Dataset	Date	Instrument	Filter	Exposure Time (s)	Final Pixel Size (")	Program
SN 1999ev							
Pre-explosion	U2JF0101/02T/03T	1995 Feb 5	WFPC2/WF2	F555W	280	0.1	5741 ¹
Post-explosion	J8DT03010	2001 Dec 31	ACS/WFC1	F555W	450	0.05	9353 ²
	J8DT03020	2001 Dec 31	ACS/WFC1	F814W	450	0.05	9353
	J8DT03030	2001 Dec 31	ACS/WFC1	F435W	400	0.05	9353
Late-time	JB4T01010	2010 Nov 14	ACS/WFC1	F555W	1368	0.035	11675 ³
	JB4T01020	2010 Nov 14	ACS/WFC1	F814W	1408	0.035	11675
	JB4T01030	2010 Nov 14	ACS/WFC1	F435W	1608	0.035	11675
SN 2003gd							
Pre-explosion	U8IXCA01M/02M	2002 Aug 25	WFPC2/WF2	F606W	1000	0.1	9676 ⁶
	U8IXCY01M/02M/03M	2002 Aug 28	WFPC2/WF2	F606W	2100	0.1	9676
Post-explosion	J8NV01020	2003 Aug 1	ACS/HRC	F435W	2200	0.025	9733 ⁵
	J8NV01040	2003 Aug 1	ACS/HRC	F555W	1000	0.025	9733
	J8NV01050	2003 Aug 1	ACS/HRC	F814W	1350	0.025	9733
Late-time	JB4T02010	2010 Nov 14	ACS/WFC	F555W	1364	0.035	11675 ³
	JB4T02020	2010 Nov 14	ACS/WFC	F814W	1398	0.035	11675
	JB4T02030	2010 Nov 14	ACS/WFC	F435W	1600	0.035	11675
SN 2004A							
Pre-explosion	U6EAD001R/02R	2001 Jul 2	WFPC2/WF3	F814W	460	0.1	9042 ⁴
	U6EAD003R/04R	2001 Jul 2	WFPC2/WF3	F606W	460	0.1	9042
Post-explosion	J8NV03010	2004 Sep 23	ACS/WFC1	F435W	1400	0.05	9733 ⁵
	J8NV03020	2004 Sep 23	ACS/WFC1	F555W	1509	0.05	9733
	J8NV03030	2004 Sep 23	ACS/WFC1	F814W	1360	0.05	9733
Late-time	JB4T03010	2010 Sep 09	ACS/WFC	F555W	1400	0.035	11675 ³
	JB4T03020	2010 Sep 09	ACS/WFC	F814W	1434	0.035	11675
	JB4T03030	2010 Sep 09	ACS/WFC	F435W	1636	0.035	11675
SN 2005cs							
Pre-explosion	J97C5	2005 Jan 20-21	ACS/WFC	F435W	2720	0.035	10452 ⁷
	J97C5	2005 Jan 20-21	ACS/WFC	F555W	1360	0.035	10452
	J97C5	2005 Jan 20-21	ACS/WFC	F658N	2720	0.035	10452
	J97C5	2005 Jan 20-21	ACS/WFC	F814W	1360	0.035	10452
Post-explosion	J9AR01011-31	2005 Jul 24	ACS/HRC	F555W	1944	0.025	11675
Late-time	JB4T04010	2010 Jul 30	ACS/WFC1	F555W	1460	0.035	11675
	JB4T04020	2010 Jul 30	ACS/WFC1	F814W	1494	0.035	11675
	JB4T04030	2010 Jul 30	ACS/WFC1	F435W	1696	0.035	11675
SN 2006my							
Pre-explosion	U2DT0901T/02T/03T	1994 May 20	WFPC2/WF2	F555W	660	0.1	5375 ¹⁰
	U2DT0904T/05T/06T	1994 May 20	WFPC2/WF2	F814W	660	0.1	5375
Post-explosion	U9OX0301M/02M/03M/04M	26 Apr 2007	WFPC2/PC	F555W	1200	0.05	10803 ¹¹
	U9OX0305M/06M	26 Apr 2007	WFPC2/PC	F814W	1200	0.05	10803
	U9OX0307M/08M	26 Apr 2007	WFPC2/PC	F450W	1400	0.05	10803
Late-time	JBKS01010	21 Nov 2010	ACS/WFC	F555W	1090	0.05	12282 ¹²
	JBKS01020	21 Nov 2010	ACS/WFC	F814W	1090	0.05	12282

¹ P.I. J. Westphal² P.I. S.J. Smartt³ P.I. J.R. Maund⁴ P.I. S.J. Smartt⁵ P.I. S.J. Smartt⁶ P.I. J. Rhoads⁷ P.I. S. Beckwith⁸ P.I. Filippenko⁹ P.I. M. Meixner¹⁰ P.I. V. Rubin¹¹ P.I. S.J. Smartt¹² P.I. D. Leonard

concern for conducting image subtraction analysis using HST images is the effect of the degree by which the PSF is subsampled. Subsampling of the PSF means that the majority of the flux in *WFPC2* images will fall in a single pixel, which may induce systematic errors in the construction of the convolution kernel. In order to assess the systematic uncertainty associated with the degree of subsampling, iterations of the image subtraction routine were conducted with different degrees of Gaussian smoothing applied to the input and/or reference images. We conservatively estimate that the total systematic uncertainties associated with the image subtraction process are $\sim 5 - 10\%$ of the flux observed in the difference image (as discussed in Section 3; with the larger systematic uncertainty associated with the fainter progenitors, in addition to the commensurate increase in the relative Poisson noise). The systematic uncertainties dominate over the Poisson noise, and we assume dominate over other noise sources, such as read noise, that are propagated to the difference images.

As we are concerned with pre-explosion and late-time images acquired with HST, the image subtraction process will involve CTI in both the input and reference images. There are two key issues with the evaluating the effect of CTI on photometry that has been derived using difference imaging: 1) the CTI that affects the progenitor flux is in the flux system of the pre-explosion image, whereas the photometry of the progenitor from the difference image is found in the flux system of the late-time reference image; and 2) the evaluation of CTI for a source using its photometry from the pre-explosion image explicitly undermines any increase in the precision of photometry that might be derived using image subtraction techniques.

For both *WFPC2* and *ACS/WFC* the CTI is principally dependent on the flux of the object, the level of the nearby background, the position of the object on the chip (the number of charge transfers to be made to readout the electrons) and the date at which the observations were made. Rather than attempting to explicitly calculate the counts associated with the progenitor on the pre-explosion image, we instead use photometry of nearby or artificial stars, in the vicinity of the progenitor, to serve as proxies for the calculation of the CTI for the progenitor. As these stars are at approximately the same position on the chip, on similar backgrounds as the progenitor and observed at the same epoch, we can reduce the problem of determining the CTI to just the dependence on the brightness (or magnitude) of the progenitor. The nearby stars (real or fake) sample a range of brightnesses and simple expressions can be derived relating the magnitude of an object in the difference image to the CTI (in magnitudes) directly.

We can consider the flux measured on the images, uncorrected for CTI, as f' . The flux corrected for CTI is then simply:

$$f = f' 10^{-0.4CTI} \quad (1)$$

Under the assumption that the CTI is a relatively small effect, we use the initial approximation that $m \approx m'$ to derive the CTI in the pre-explosion frame using photometry, derived from difference images, in the photometric system of the pre-explosion images.

On the *ACS* images, we model the CTI as being effectively dependent on only two parameters: the brightness of the object and its y -position on the *FLT* images. We established, for the images considered here, that the effect of nearby background inhomogeneities, around the progenitor positions, are well within the stated uncertainties of the CTI expressions. We consider the CTI for a given range of pixels to be approximately given by a power law dependent only on the magnitude of the object:

$$CTI(m) = \beta m^\alpha \quad (2)$$

We evaluated the coefficients of Equation 2 for each pre-explosion *ACS/WFC* image (as the coefficients are dependent on the date on which the observations were made and the specific background at the progenitor position), using real and artificial stars for which the CTI had been evaluated using the equations of Chiaberge et al. (2009). Due to significant uncertainty in the expression used to determine the CTI, and its slowly varying nature with pixel position, it is possible to consider the CTI to be approximately fixed over ~ 50 pixel ranges in y .

We make a similar approximation for the *WFPC2* observations, using the CTI formulation presented by Dolphin (2000a)⁷, derived using artificial stars generated using *HSTphot*. We find the average dependence of the CTI (over a 50 pixel range in y -position) to correspond to a second order polynomial:

$$CTI(m) = \alpha + \beta m + \gamma m^2 \quad (3)$$

For both *WFPC2* and *ACS* observations, the dependence on m is relatively weak; the difference in its evaluation using m or m' is negligible. The importance of this approach is that it avoids specifically determining fluxes and sky background values from the pre-explosion images (which defeats both the purpose and precision afforded by using image subtraction techniques to derive the photometry of the pre-explosion source). The zeropoint in the photometric scale of the reference image Z_R can be derived from photometry m_R of reference stars, identified by *ISIS*. Using a package such as *ISIS*, f'_R of the reference objects in the reference image can be measured directly using aperture photometry and can be compared directly with the photometry of the same stars derived using *DAOPHOT*, *DOLPHOT* or *HSTphot*; such that Z_R contains not only the absolute zeropoint, but also all the relevant aperture corrections. The magnitude m_d of the progenitor candidate can then be found directly. As the image subtraction procedure determines the difference in observed fluxes f' , these fluxes must be further corrected for CTI derived on the input image (containing the progenitor) using the scheme outlined above. Given the difference measured from reference and input images, the final magnitude of the pre-explosion source is given as:

$$m_d = -2.5 \log_{10}(f'_d) + Z_R + CTI_i \quad (4)$$

An additional source of systematic uncertainty is the differences in the filter transmission functions between images used for image subtraction analysis. We note that, although some filters are nominally identical, there may also be differences between the same filters used on different instruments. We used synthetic photometry of *ATLAS9* (Castelli & Kurucz 2004) and *MARCS* (Gustafsson et al. 2008) model SEDs, using the total transmission (filter and instrument) functions, to determine the relative colour differences between the filter sets used here. For most combinations of filters, in particular between nominally identical HST filters, the colour difference as a function of temperature is < 0.1 mags for low reddening (see Fig. 1).

2.7 Non-detections and detection limits

In previous studies (e.g. Maund & Smartt 2005; Crockett et al. 2011), the derivation of the detection thresholds has been conducted using analytical expressions for the background and source

⁷ with updates from <http://purcell.as.arizona.edu/wfpc2.calib/>

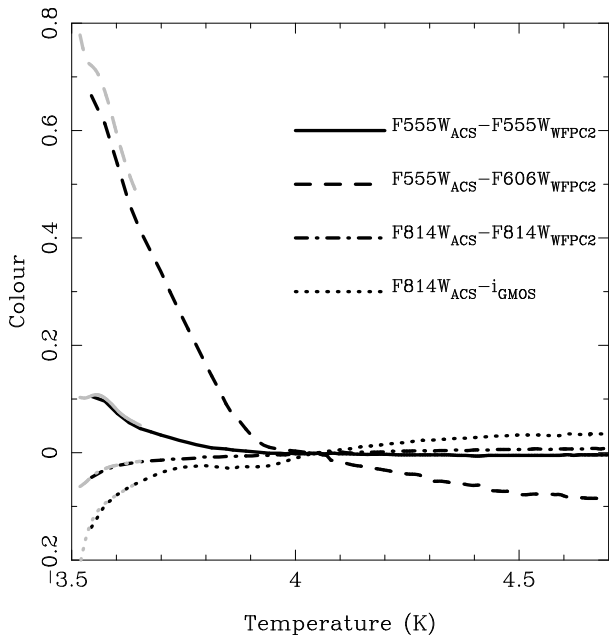


Figure 1. Colour terms, between filter sets, as a function of temperature for ATLAS9 (heavy lines; Castelli & Kurucz 2004) and MARCS (grey line; Gustafsson et al. 2008) model SEDs (appropriate for supergiants with $E(B-V) = 0$; see Section 4).

noise for an “ideal” observation. This approach, however, does not accurately reflect the way in which stars are actually detected in the photometry process, using IRAF tasks such as DAOFIND, and the effect of crowding. We consider the insertion and attempted recovery of artificial stars to derive the detection threshold.

Artificial stars were generated using the PSFs derived from the data themselves, with a randomly selected magnitude from a uniform distribution and with a position uniformly distributed within ± 0.5 px in x and y of the SN location. The first approach involved repeating the original detection and aperture and PSF photometry routine on the pre-explosion images, with artificial stars inserted, and considering a detection to be any recovery of a star within 1 pixel and 0.5 magnitudes of the input star’s parameters. The second approach utilised ISIS to conduct image subtraction between the late-time images and pre-explosion images, in which artificial stars had been inserted in the latter. For this latter approach, we set the coordinates at which ISIS was to conduct aperture photometry and classified a detection to be any instance in which the recovered flux was 3 times that of the corresponding noise (including the systematic uncertainty; see section 2.6).

We consider the detection threshold to be the magnitude at which we recover 50% of input artificial stars, using a 3σ detection threshold with DAOPHOT. As noted by Maud (2013, in prep.), the completeness function can be considered in terms of the complementary cumulative Gaussian distribution. We therefore quote the corresponding width of the completeness function as an effective uncertainty on the derived detection threshold.

3 OBSERVATIONAL RESULTS

3.1 SN 1999ev

SN 1999ev was discovered by T. Boles (Hurst et al. 1999) on 1999 Nov 7.225 in the galaxy NGC 4274. Garnavich et al. (1999) sub-

sequently classified the SN as being of Type II, although no further sub-classification of the SN has been reported. Van Dyk et al. (2003a) attempted to identify the progenitor object in pre-explosion WFPC2 $F555W$ images from 1995 Feb 1, although were not able to conclusively identify a single object as the progenitor. In an independent analysis, using a differential astrometric solution derived using post-explosion ACS WFC images containing the SN, Maud & Smartt (2005) were able to identify a star in the pre-explosion images coincident with the SN position (with an uncertainty of $0.02''$).

Late-time ACS WFC $F435W$, $F555W$ and $F814W$ images (with pixel scale $0.035'' \text{ px}^{-1}$) of the site of SN 1999ev were acquired on 2010 Nov 14 (11 years post-discovery). A late-time image of the site of SN 1999ev is shown as Fig. 2. A geometric transformation was calculated between the post-explosion and late-time $F555W$ images using 24 common stars, with an uncertainty on the transformation of $\Delta r = 0.016''$. A source is recovered in the late-time images at the transformed position of the SN as identified in the post-explosion images by Maud & Smartt (2005), as shown in Fig. 3. The source is detected in all three filters: $m_{F435W} = 25.63 \pm 0.07$, $m_{F555W} = 24.76 \pm 0.06$ and $m_{F814W} = 23.65 \pm 0.05$. The photometry of the SN in the post-explosion images was recalculated, and the SN was measured to have $m_{F435W} = 24.79 \pm 0.10$, $m_{F555W} = 24.19 \pm 0.14$ and $m_{F814W} = 23.49 \pm 0.10$. We note that the new measurement of the post-explosion $F555W$ photometry reported here is slightly fainter than measured previously, although the $F435W$ and $F814W$ magnitudes are approximately similar to those of Maud & Smartt (2005). The 8.98 years between the post-explosion and late-time images reveals significant evolution in the light echo discovered by Maud & Smartt (2005), which has expanded to a radius of $0.48''$ from $0.25''$ (as shown on Figs. 3 and 4).

A transformation was calculated between the post-explosion and pre-explosion $F555W$ images using 24 stars (with a transformation uncertainty of $\Delta r = 0.039''$). In the pre-explosion images, we identify the same source that Maud & Smartt (2005) identified as the progenitor source with $m_{F555W} = 24.66 \pm 0.17$. In addition, we also find a nearby source with $m_{F555W} = 25.08 \pm 0.24$ located $0.2''$ (2 WF pixels) from the progenitor. We note that, for the period in which the pre-explosion observations were conducted⁸, the nearest logged warm pixel is 5 pixels away from the SN position and not coincident with either the progenitor candidate or the nearby object. In the late-time image, however, we do not recover any source at the corresponding transformed position. The position of the pre-explosion source at the SN position was estimated using the three centring algorithms available to DAOPHOT (centroid, Gaussian and optimal filter) and the position determined using HSTPHOT PSF fitting. The positions are shown, with respect to the transformed position of the SN on the pre-explosion image, in Fig. 5. Although there is an apparent discrepancy in the positions for the source and the transformed SN position, the discrepancy is not significant. It does, however, raise concerns about how positions are determined on subsampled images such as this pre-explosion WFPC2 WF2 $F555W$ image. The position determined using the optimal filter centring algorithm is noticeably different from the other three positions derived from the pre-explosion image and is offset in the direction of the nearby apparent neighbouring star. The standard deviation of the four measurements made on the pre-explosion image is $0.022''$. Given the apparent brightness

⁸ http://www-int.stsci.edu/ftp/instrument_news/WFPC2/Wfpc2_hotpix/1995/vary_950113_950211_2.dat.Z

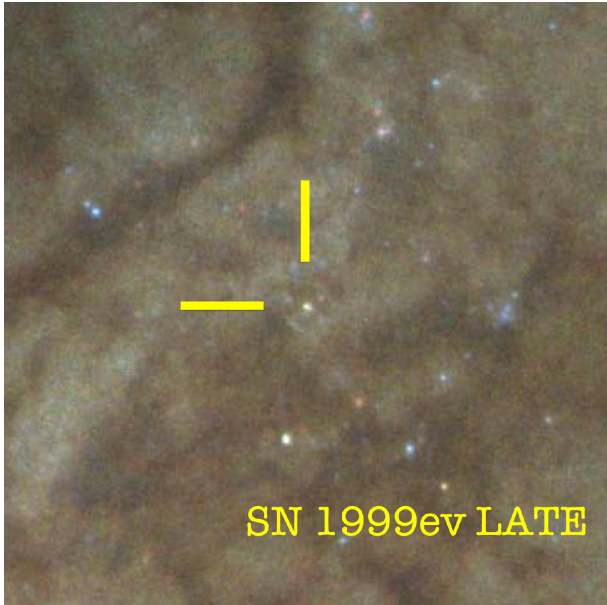


Figure 2. Late-time colour image (composed of $F435W$, $F555W$ and $F814W$ images) of the area of NGC 4274 containing SN 1999ev. The image has dimensions $15'' \times 15''$, and is oriented such that North is up, and East is left. The position of SN 1999ev is located at the centre of the image.

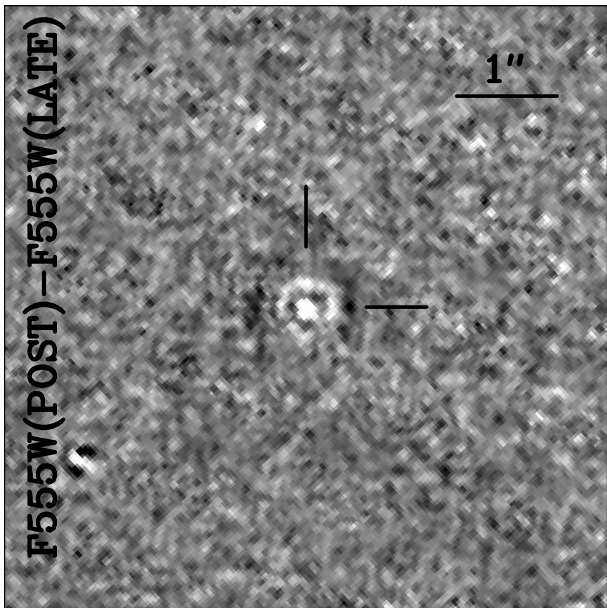


Figure 4. Difference image between the post-explosion and late-time $F555W$ observations of the site of SN 1999ev. The evolution of the expanding light echo is evident; the white echo appears in the post-explosion image, while the outer dark echo occurs in the late-time frame.

of the source, however, the astrometric uncertainty for the position derived using HSTphot alone may be as large as $0.04''$ or 0.4 WF pixels (Dolphin 2000b).

3.2 SN 2003gd

SN 2003gd was discovered by R. Evans on 2003 Jun 12.82, in the galaxy M74 (Evans & McNaught 2003). Kotak et al. (2003)

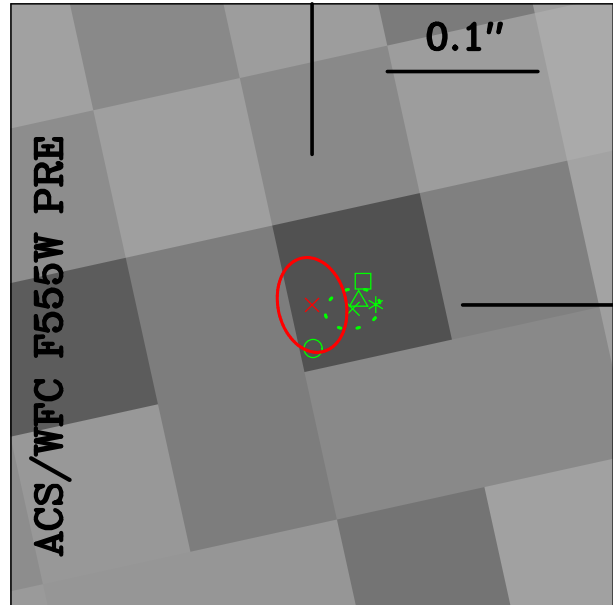


Figure 5. Close-up of the pre-explosion site of SN 1999ev. In red (\times) is the transformed position of the SN, derived from the post-explosion images, and the corresponding r.m.s. error ellipse. Also shown (in green) are the four separate measures of the position of the pre-explosion source derived using the centroid (\square), Gaussian (\triangle) and optimal filter (\circ) centring algorithms in DAOPHOT and the position determined using HSTphot ($*$). Also shown are the average (\times) and the corresponding standard deviation ellipse of the four measurements.

spectroscopically classified 2003gd as being a Type II SN, approximately 2 days post-explosion. Subsequent photometric and spectroscopic observations of SN 2003gd, however, showed it to be a Type IIP SN discovered at the end of the plateau phase (Hendry et al. 2005). Smartt et al. (2003) made a preliminary identification of the progenitor in pre-explosion *HST* WFPC2 $F606W$ and Gemini GMOS-N i' images. As such, SN 2003gd was the third SN, after SNe 1987A and 1993J, to have a progenitor identified in fortuitous pre-explosion images. Independent analyses by Smartt et al. (2004) and Van Dyk et al. (2003b) showed the candidate progenitor to be a RSG, corresponding to a star with initial mass of $\sim 8 - 9 M_{\odot}$. The confirmation of this star as the progenitor was finally provided in 2009, when the star was observed to no longer be present in late-time Gemini GMOS-N i' images (Maund & Smartt 2009); making it the first conclusively confirmed RSG progenitor for a Type IIP SN.

Late-time ACS *WFC* observations of the site of SN 2003gd were acquired on 2010 Nov 14, and are presented on Figure 6. The SN position in the late-time images was determined with respect to the ACS HRC post-explosion images, with an uncertainty on the transformation of $0.010''$. The position of the SN on the pre-explosion *HST* and Gemini images, as presented by Smartt et al. (2004) and Maund & Smartt (2009), were recalculated to within $0.028''$ and $0.025''$ respectively. The pre-explosion, post-explosion and late-time data $F555W$ images are shown on Figure 7 and, for completeness, we also show the corresponding i' data presented by Maund & Smartt (2009) as Figure 8.

In the late-time images we observe a source, termed Source A' , that is clearly recovered in all late-time *HST* images at the transformed SN position, with magnitudes 25.93 ± 0.04 , 25.42 ± 0.05 and 24.90 ± 0.04 in the $F435W$, $F555W$ and $F814W$ filters respectively. This source was detected in late-time Gemini GMOS-N g' and r'

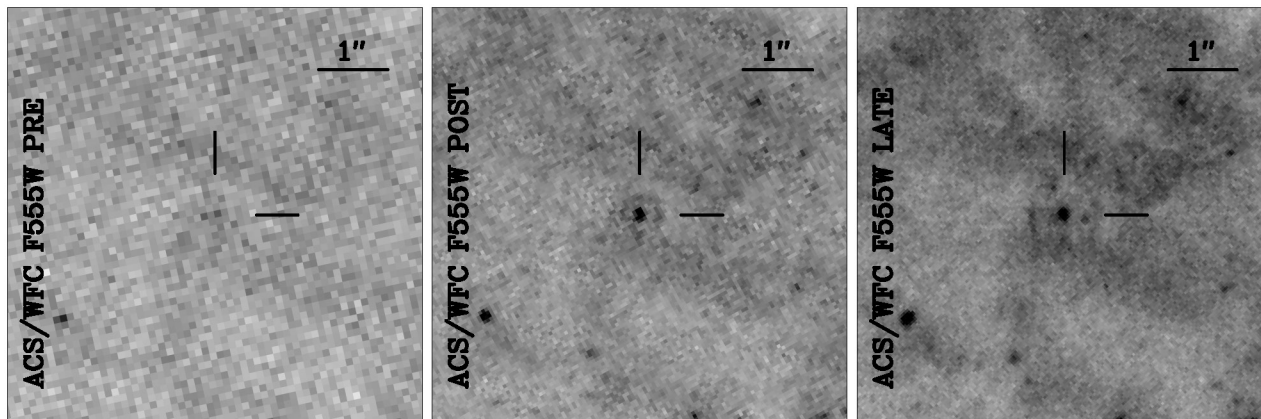


Figure 3. HST imaging of the site of SN 1999ev. From left to right: Pre-explosion WFPC2 WF2 *F555W* image; Post-explosion ACS/WFC *F555W* image; and late-time ACS/WFC *F555W* image.

images, but not recovered significantly in the corresponding i' image, acquired on 2008 Sep 06. Maund & Smartt (2009) measured $g' = 25.10 \pm 0.04$ and $r' = 24.49 \pm 0.05$ (in Vega magnitudes) for the source at the SN position, and placed a detection limit of $i' > 25.9$. This source was also observed with *HST* WFPC2 on 2007 Aug 11 (for program *GO* – 11229; PI: M. Meixner). Photometry of these images using the HSTphot package yielded $m_{F622W} = 24.52 \pm 0.08$ and $m_{F814W} = 25.22 \pm 0.26$. We note that this photometry is approximately 0.4 magnitudes brighter than the photometry of the same images reported by Otsuka et al. (2012). We confirmed our photometry using ISIS, determining the flux difference between the source in the 2007 WFPC2 *F814W* image and our late-time ACS *F814W* image is consistent with the photometry conducted on the images directly.

We recalculated the photometry of the source at the SN position in the pre-explosion WFPC2 *F606W* image, labeled Source A by Smartt et al. (2004), using HSTphot finding $m_{F606W} = 25.06 \pm 0.06$. Maund & Smartt (2009) derived the i' magnitude of the progenitor, using image subtraction techniques (see Figure 8), of 23.85 ± 0.04 (with a possible 0.15 magnitude systematic uncertainty on underlying residual flux in the late-time Gemini image). Unlike the obviously red Source A observed in the pre-explosion *HST* WFPC2 and Gemini GMOS images, it is apparent that Source A' in the late-time images is a blue-yellow object (see Figure 6). Even taking into account a colour correction between the late-time *F814W* and Gemini GMOS i' photometry (see Fig. 1), a significant increase in brightness is evident between the two observations separated by two years.

3.3 SN 2004A

SN 2004A was discovered by K. Itagaki (Nakano et al. 2004) on 2004 Jan 9.4 in the galaxy NGC 6207. Kawakita et al. (2004) spectroscopically classified the SN as a being a young Type II SN. Hendry et al. (2006) presented photometric and spectroscopic observations of SN 2004A and showed it to be consistent with other normal Type IIP SNe, such as SN 1999em. Hendry et al. also presented an analysis of the pre-explosion *HST* WFPC2 observations of the site of SN 2004A from 2001 Jul 02, in conjunction with post-explosion ACS WFC observations of the SN acquired on 2004 Sep 23. A source was barely recovered at 4.7σ at the SN position in the pre-explosion *F814W* image. There was no corresponding source in the pre-explosion *F606W* image, consistent with a star

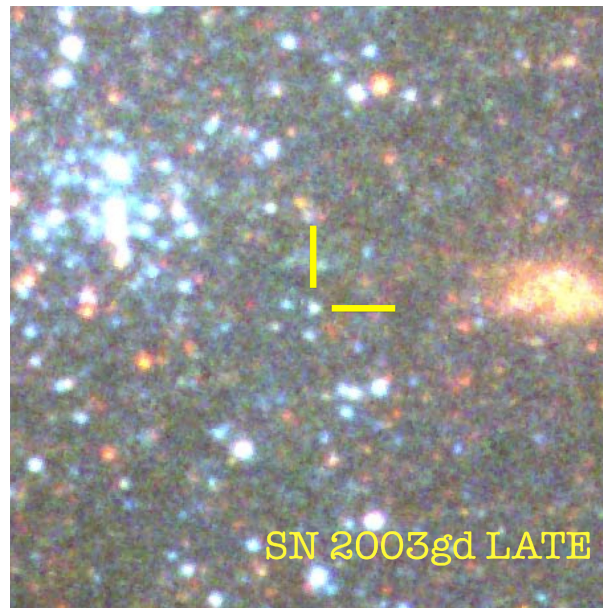


Figure 6. Late-time colour image (composed of *F435W*, *F555W* and *F814W* images) of the area of M74 around the site of SN 2003gd. The image has dimensions $8'' \times 8''$, and is oriented such that North is up, and East is left. The position of SN 2003gd is located at the centre of the image.

with $F606W - F814W > 1.05$. Hendry et al. concluded that if this was the progenitor star an RSG with initial mass $9_{-2}^{+3} M_{\odot}$; although given concerns about the significance of the detection of the source at the SN position, Hendry et al. placed a conservative limit on the initial mass of an undetected progenitor of $< 12 M_{\odot}$.

Late-time observations of the site of SN 2004A were acquired on 2010 Sep 09, approximately 6.7 years post-discovery. The late-time *F814W* observation and the corresponding pre-explosion *F814W* observation are presented on Figure 9. The pre-explosion and late-time observations of the site of SN 2004A are presented in Figure 9. Using the post-explosion *F814W* image, acquired on 2004 Sep 23 with ACS WFC, the position of the SN on the pre-explosion and late-time frames was determined to within $0.021''$ and $0.028''$, respectively. The SN is not detected significantly in any of the late-time ACS WFC images. The 3σ detection limits at the SN position, in the late-time images, were evaluated with artificial

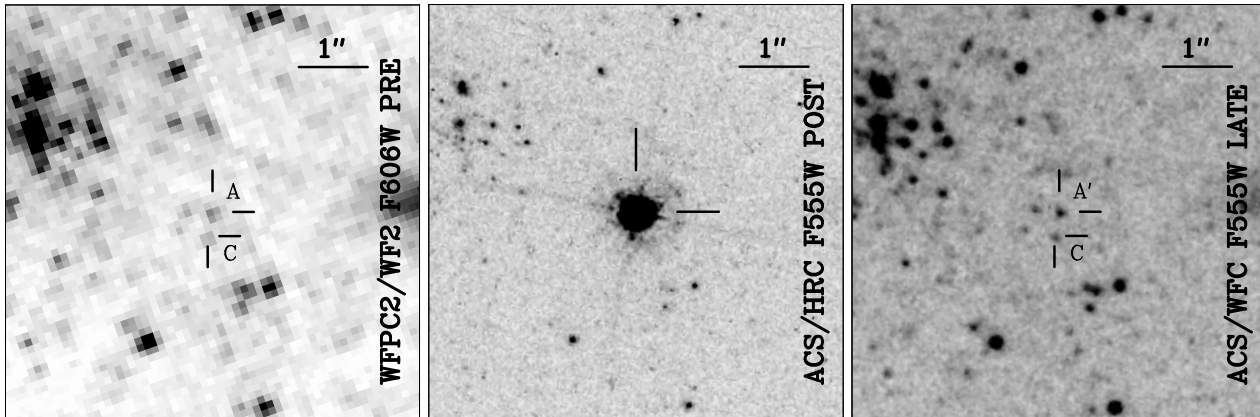


Figure 7. HST imaging of the site of SN 2003gd. From left to right: Pre-explosion WFPC2 WF2 F606W image; Post-explosion ACS/HRC F555W image; and late-time ACS/WFC F555W image.

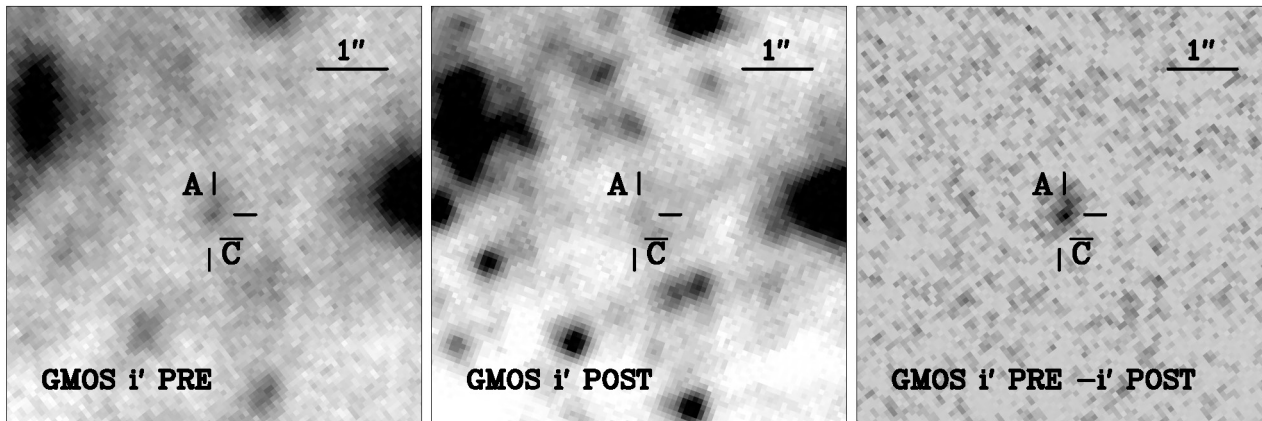


Figure 8. Pre-explosion and late-time Gemini i' observations of the site of SN 2003gd (for further details see Maund & Smartt 2009).

star tests to be $m_{F435W} = 27.65$, $m_{F555W} = 27.5$ and $m_{F814W} = 26.85$ mags. These limits are consistent with the expected depth for these images predicted by the ACS imaging exposure time calculator⁹.

In the pre-explosion $F814W$ image, HSTphot finds a source within $0.034''$ of the transformed SN position with $m_{F814W} = 24.48 \pm 0.19$ mags, detected with a signal-to-noise ratio of 5.6 (as shown on Figure 9). The positional uncertainty is slightly larger than the formal 1σ uncertainty of the geometric transformation alone. The ability of HSTphot to determine the position of objects of such brightness, however, is limited, such that the expected uncertainty on the position of the object on the pre-explosion $F814W$ image is $\Delta r \geq 0.060''$ (Dolphin 2000b). We note that this is the same object identified by Hendry et al. (2006) as the possible candidate progenitor, although they measured the source to be ~ 0.2 magnitudes brighter with a larger photometric uncertainty (we note, also, they did not correct their reported photometry to an infinite aperture, such that the discrepancy is a further 0.05 magnitudes larger). We also find the two sources A and B identified by Hendry et al. (2006) are hot pixels¹⁰. The pixel immediately adjacent to the pixel hosting the majority of the progenitor candidate's flux is a warm pixel; however this pixel has a low dark current (with

low variability)¹¹ and was corrected by the OTFR pipeline. We determined the 50% completeness level for 3σ detections for the pre-explosion images using artificial star tests conducting the HSTphot. Artificial stars were placed in a 5px radius around the transformed SN position. We find the corresponding detection limits to be $m_{F606W} = 26.25 \pm 0.40$ and $m_{F814W} = 25.10 \pm 0.45$ mags.

The late-time $F814W$ image was subtracted from the pre-explosion image, and the difference images is presented on Fig. 9. We find residuals at the location of the progenitor source and the two hotpixels. The disappearance of the pre-explosion progenitor candidate in these late-time images confirms the authenticity of the object as the progenitor. We derived photometry of the residual at the transformed SN position of $m_{F814W} = 24.57 \pm 0.12$ mags, including a systematic uncertainty of $\sim 10\%$. Using the results from the artificial star tests, we derived a CTI correction of -0.216 ± 0.013 , yielding a final magnitude for the progenitor of $m_{F814W} = 24.36 \pm 0.12$ mags. This is similar to the photometry derived by Hendry et al. (2006), although for very different reasons and improved precision.

A similar difference image was determined for the pre-explosion $F606W$ image and the late-time $F555W$ image. No significant residual was found in the difference image as expected,

⁹ <http://etc.stsci.edu/etc/input/acs/imaging/>

¹⁰ http://www.stsci.edu/hst/wfpc2/analysis/wfpc2_hotpix.html

¹¹ http://www-int.stsci.edu/instruments/wfpc2/Wfpc2_hotpix/2001/vary_010617_010711_3.dat.Z

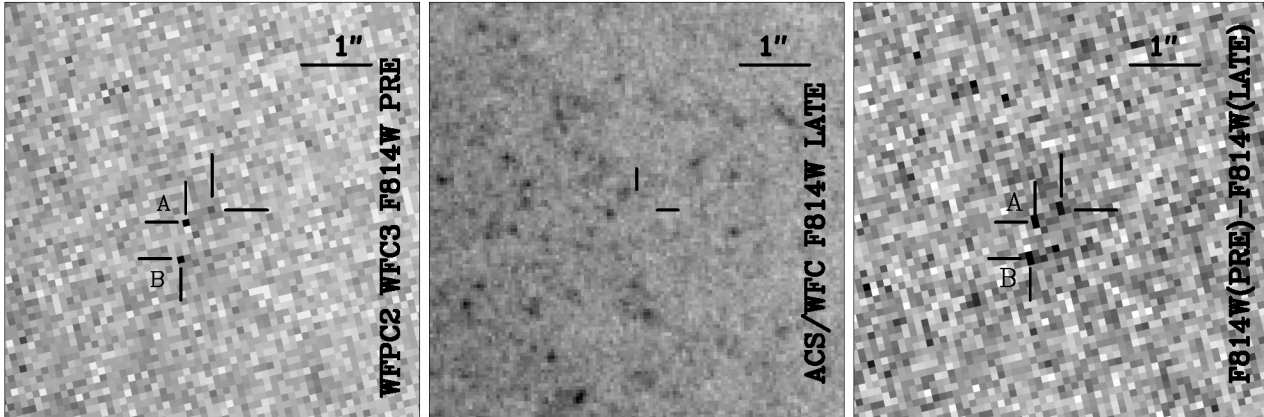


Figure 9. The site of SN 2004A in NGC 6207. Left) Pre-explosion WFPC2 $F814W$ image from 2001 Jul 02 with scale $0.1'' \text{ px}^{-1}$. The centred cross hairs mark the transformed position of SN 2004A and the nearby sources A and B are known hot pixels on the WFPC2 WF2 chip. Centre) Late-time ACS/WFC $F814W$ image. Right) Difference image between the late and pre-explosion $F814W$ images. The observed residual sources correspond to the two hot pixels, A and B, and the progenitor.

given the absence of a source at the transformed SN position in the pre-explosion image. Due to differences between the pre-explosion $F606W$ and late-time $F555W$ filter transmission functions, we did not use the difference image to derive detection limits for the progenitor.

3.4 SN 2005cs

SN 2005cs was discovered by Kloehr et al. (2005) on 2005 Jun 27.933 in the galaxy M51. Modjaz et al. (2005) spectroscopically classified SN 2005cs as being a young Type II SN. Richmond & Modjaz (2005) provisionally identified a blue supergiant in the field as a possible candidate for the progenitor, although later analysis (in conjunction with high resolution post-explosion HST ACS HRC images) by Maund et al. (2005) and Li et al. (2006a) found the progenitor star to be a RSG with initial mass $M_{ZAMS} \sim 8M_{\odot}$.

Late-time observations of the site of SN 2005cs were acquired on 2010 Jul 30 with the ACS/WFC, 5.1 years post-discovery. A comparison of the pre-explosion and late-time observations of the site of SN 2005cs is shown as Figs. 10 and 11. In this case, the late-time observations exactly match the pre-explosion observations, using the same filters and detectors. The pre-explosion and late-time observations were drizzled to a final common pixel scale of $0.035''$. Utilising post-explosion ACS HRC observations of SN 2005cs, the SN position was located on the pre-explosion and late-time images to within $0.007''$ and $0.004''$, respectively.

Direct photometry of the source detected at the SN position in the pre-explosion $F814W$ yielded $m_{F814W} = 23.382 \pm 0.048$, which is 0.1 magnitude fainter than reported by Maund et al. (2005), but ~ 0.3 magnitudes brighter than reported by Li et al. (2006b). In the late-time images, we do not recover a source at the transformed SN position. The detection limits in these filters were probed using artificial star tests, yielding $m_{F435W} = 24.30 \pm 0.4$, $m_{F555W} = 24.95 \pm 0.45$ and $m_{F814W} = 24.55 \pm 0.15$ mags. These limits are particularly high, relative to the expected depth for ACS/WFC images of these durations, due to extended emission from the nearby cluster overlapping SN position.

As noted by Maund et al. (2005) and Li et al. (2006b), this underlying emission can complicate the determination of the photometry of the progenitor from the pre-explosion imaging alone. This highlights the importance of using image subtraction techniques

to accurately derive the progenitor photometry (by subtracting the background emission that is constant at both epochs). The difference image between the pre-explosion and late-time $F814W$ observations is presented on Fig. 11. We measure the brightness of the progenitor to be $m_{F814W} = 23.62 \pm 0.07$ mags, which is fainter than the brightness determined from direct photometry of the pre-explosion source (see above). This magnitude is also significantly fainter than the photometry of Maund et al. (2005), and slightly brighter than the photometry of Li et al. (2006a) (who attempted to account for pre-explosion flux at the SN position due to the nearby cluster). We note that we find no significant source at the SN position in the corresponding $F435W$ and $F555W$ difference images.

Artificial star tests, in conjunction with image subtraction techniques, were used to derive alternative detection limits (see Section 2.7) for the pre-explosion $F435W$ and $F555W$ images. In the absence of a corresponding late-time $F658N$ ACS/WFC image, the detection limit on the pre-explosion $F658N$ image could only be derived using direct recovery of artificial stars on the pre-explosion frame. The photometric completeness functions for the pre-explosion observations in which the progenitor was not detected is shown on Fig. 12 and presented in Table 3. The detection of a residual in isis difference images requires only a significant degree of residual flux at the SN position and is less dependent on the amount of background flux than the direct recovery of artificial stars. There are differences between the detection limits derived on the pre-explosion images here and the limits presented by Maund et al. (2005) and Li et al. (2006b). These studies used combinations of the analytical noise expression and artificial star tests, and treated the effect of flux from the nearby cluster differently. We note that our detection limits derived using image subtraction techniques are significantly deeper, highlighting the importance of late-time images even in cases where detections of the progenitor are dubious or unavailable.

We also find that there are a number of other sources that are clearly variable between the pre-explosion and late-time images in the vicinity of SN 2005cs (as shown on Fig. 11). Inspection of the pre-explosion and late-time images shows that the apparent residuals in the difference images are associated with stars which are clearly brighter or fainter in the late-time images compared with the pre-explosion images. Given the density of stars in this field, compared with the sites of the other SNe considered here, it is to

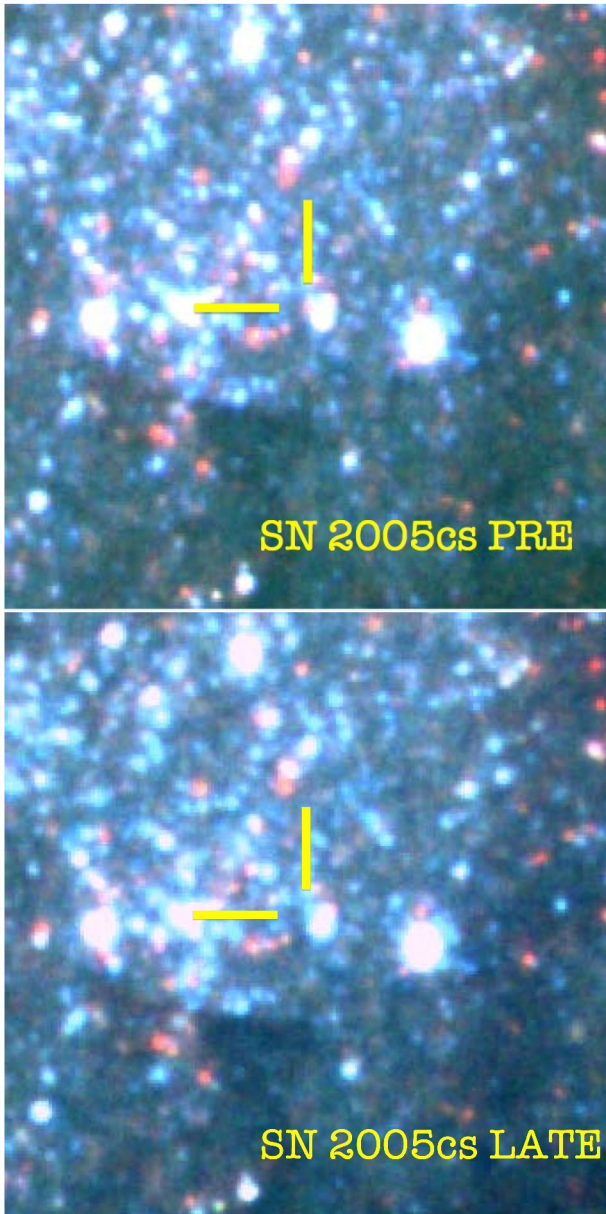


Figure 10. Colour images of the site of SN 2005cs using ACS/WFC before explosion and at late-times. The position of the SN is indicated by the cross-hairs. In the pre-explosion image a red source is clearly visible at the SN position, and is found to be absent in the late-time image. Each image has dimension $6'' \times 6''$, and is oriented such that North is up, East is left.

be expected that there would be other variable sources in the field around SN 2005cs. The other residuals in the difference images are, therefore, consistent with other real variables, but the progenitor object is the only star to be absent in one of the two sets of the images.

3.5 SN 2006my

SN 2006my was discovered on 2006 Nov 8.82UT by K. Itagaki (Nakano & Itagaki 2006) in the galaxy NGC 4651. Stanishev & Nielsen (2006) spectroscopically classified the SN as being a Type II SN similar to SN 1999em. Li et al. (2007), Leonard et al. (2008) and Crockett et al. (2011) analysed the pre-explosion WFPC2 im-

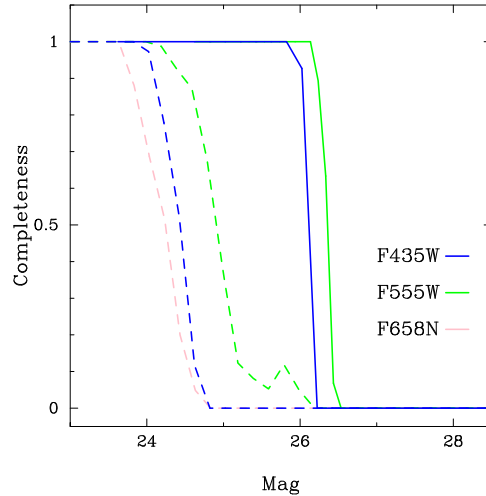


Figure 12. Detection completeness functions for pre-explosion ACS/WFC observations of the site of SN 2005cs for the $F435W$, $F555W$ and $F658N$ filters (in which the progenitor was not detected). The dashed curves indicate the completeness functions derived from attempted direct recovery of artificial stars on the original pre-explosion images, while solid curves are for detection limits derived in conjunction with image subtraction techniques.

Table 3. Detection limits for pre-explosion ACS/WFC $F435W$, $F555W$ and $F658N$ images of the site of SN 2005cs measured using artificial star tests and direct recovery and image subtraction techniques. Previously derived detection limits from Maund et al. (2005) and Li et al. (2006b) are shown for comparison

	Recovery	ISIS	Maund et al.	Li et al.
$F435W$	24.35 ± 0.20	25.8 ± 0.1	24.8	...
$F555W$	24.85 ± 0.30	26.4 ± 0.1	25	25.6
$F658N$	24.15 ± 0.30

ages of the site of SN 2006my. All three studies commented on the significant offset between the transformed SN position and a nearby source recovered in the pre-explosion $F814W$ image. Leonard et al. and Crockett et al. concluded that the $F814W$ source was unrelated to the SN, and that the progenitor was not detected in either the pre-explosion $F555W$ or $F814W$ images.

The pre-, post-explosion and late-time $F555W$ and $F814W$ imaging of the site of SN 2006my is shown on Fig. 13. Following the analyses presented by Li et al. (2007), Leonard et al. (2008) and Crockett et al. (2011), we analysed the pre-explosion WFPC2 WF2 $F555W$ and $F814W$ covering the position of SN 2006my. The SN position, derived from post-explosion WFPC2 PC1 images, was determined on the pre-explosion images using 19 common stars with a resulting uncertainty of $0.024''$; larger than achieved by Crockett et al. (2011). The transformed position is found to be in the proximity of a cluster of bright pixels and, as previously found by Li et al. (2007), Leonard et al. (2008) and Crockett et al. (2011), the transformed position is not consistent with the position of the nearest source found by HSTphot in the pre-explosion $F814W$ image (see Fig. 13). The source detected by HSTphot is located 0.97 pixels from the transformed SN position, an offset significantly larger than the transformation uncertainty. The transformed SN position is close to the position of a source in the pre-explosion $F555W$ image but, as noted by the previous studies, based on the sharpness

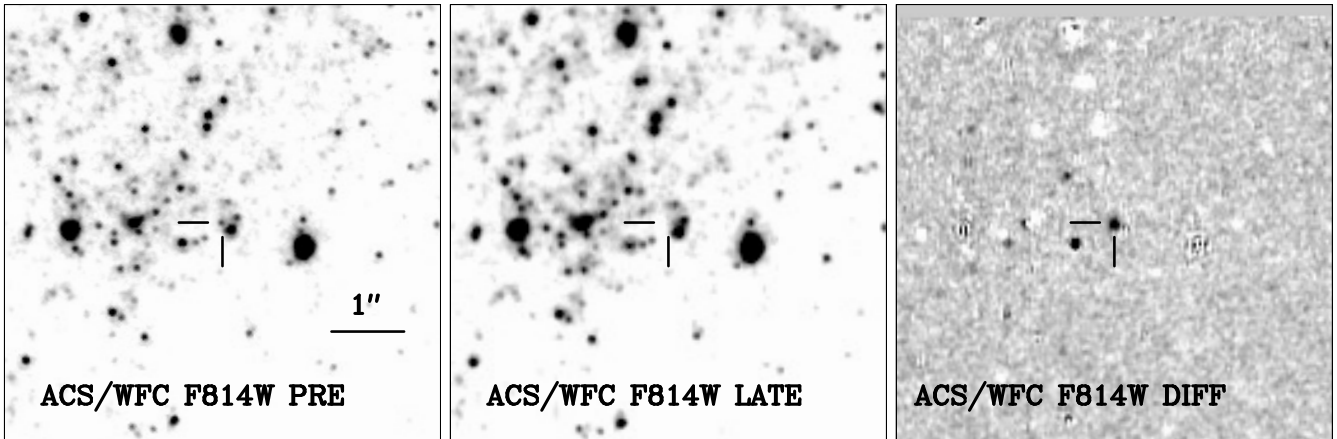


Figure 11. ACS WFC $F814W$ observations of the site of SN 2005cs. Left) Pre-explosion $F814W$ image (0.44 years prior to discovery). The cross hairs indicate the transformed position of the SN and the identified progenitor candidate. Centre) Late-time $F814W$ image (5.09 years post-discovery) with the progenitor candidate absent. Right) Difference image, between the pre-explosion and late-time $F814W$ observations, clearly showing a residual at the SN position.

value derived by HSTphot, it is not consistent with a point source and is located 1.19 pixels from the source detected in the $F814W$ image. The shift between the pre-explosion $F555W$ and $F814W$ image was found to be very small: $\Delta x = -0.0039$ and $\Delta y = 0.0395$.

Using HSTphot, the pre-explosion $F814W$ source was measured to have brightness 24.24 ± 0.18 , which is approximately 0.2 magnitudes brighter than found in the previous studies (which is due to the use of different HSTphot settings used here). Sections of the late-time $F555W$ and $F814W$ images were transformed to match the pre-explosion images; resampling the ACS WFC 0.05'' pixels to 0.1''. These images were processed using ISIS, and the resulting difference images are shown in Fig. 13. ISIS significantly detects a residual, at a distance of only 0.11 pixels from the transformed position of the SN. Using 5 reference stars, and the DOLPHOT photometry derived for these stars in the late-time $F814W$ image, we derive a magnitude of 24.88 ± 0.13 mags for the residual in the difference image. Artificial star tests on the pre-explosion images were used to derive the CTI correction, for a star at the position of the observed residual on the pre-explosion frame, of 0.016 ± 0.003 . The residual in the $F814W$ difference image corresponds, therefore, to an object with $m_{F814W} = 24.86 \pm 0.13$. Given the coincidence of residual with the transformed SN position, we conclude that the progenitor was detected in the pre-explosion $F814W$ image. The fainter $F814W$ magnitude derived using ISIS, compared to our own HSTphot photometry of the pre-explosion images and the previously reported values, and the apparent discrepancy in the position of the pre-explosion source and the SN, most likely reflects that the source in the pre-explosion $F814W$ image is a blend of the progenitor with a source due East of the SN position (which also skews the apparent position of the progenitor source in that direction). In the analysis of the pre-explosion and late-time $F555W$ images no residual was found in the difference image. The possible nature of the pre-explosion $F555W$ source is revealed in the late-time images as a complicated, extended background feature.

We used artificial star tests to probe the detection limit of the pre-explosion $F555W$ and $F814W$ images within a 10 pixel radius of the SN position; deriving 50% completeness limits at 3σ of $m_{F555W} = 26.15 \pm 0.65$ and $m_{F814W} = 25.05 \pm 0.75$ mags.

4 ANALYSIS

In previous studies (e.g. Maund & Smartt 2005; Smartt et al. 2004; Hendry et al. 2006; Li et al. 2006a; Maund et al. 2005), the photometric properties of the progenitor and surrounding stars were derived through comparison with the ideal supergiant colour sequence presented by Drilling & Landolt (2000). As noted by Maund (2013, in prep.) there are significant deficiencies with this approach; such as the requirement for colour transformation equations to transform the observed photometry to the photometric system of Drilling & Landolt. More recent studies (e.g. Van Dyk et al. 2012; Maund et al. 2011; Van Dyk et al. 2011; Fraser et al. 2012; Maund et al. 2013) have shown the benefit in fitting directly to SEDs constructed from synthetic spectra with known parameters using the same filters as the observations.

In considering the observed photometry of objects identified at the position of the target SN in the pre-explosion images we utilised the BIX nested sampling and BASIE Markov Chain Monte Carlo SED fitting packages described by Maund (2013, in prep.). These two packages allow us to comprehensively probe the effects of different stellar parameters on the interpretation of the observed photometry on a densely sampled grid of model stellar photometry, in the native filter system of the observations. By design, both of these SED fitting packages can handle detections and upper limits simultaneously, although for limited data (i.e. the number of detections is less than the number of free parameters) only the BASIE code can be used to explore the allowed parameter space rather than locate a unique solution. Crucially, we can explore the degeneracies between the parameters (such as temperature and reddening), and implicitly account for correlations between the temperature and bolometric luminosity (through the bolometric correction).

Here we use two families of stellar SED models: the ATLAS9 (Castelli & Kurucz 2004) and MARCS (Gustafsson et al. 2008) models. Synthetic photometry of these models was conducted using our own codes.

As we expect the progenitors to be cool RSGs ($< 4500K$), we interpret the observed photometry (and upper limits) with respect to the $5M_{\odot}$ spherical MARCS SEDs, which have been successfully compared with observations of RSGs in a number of previous studies (e.g. see Levesque et al. 2005; Davies et al. 2013). We assume that RSGs are well described by models with surface gravity $\log g = 0.0$, and fit for the effective temperature (T_{eff}) and

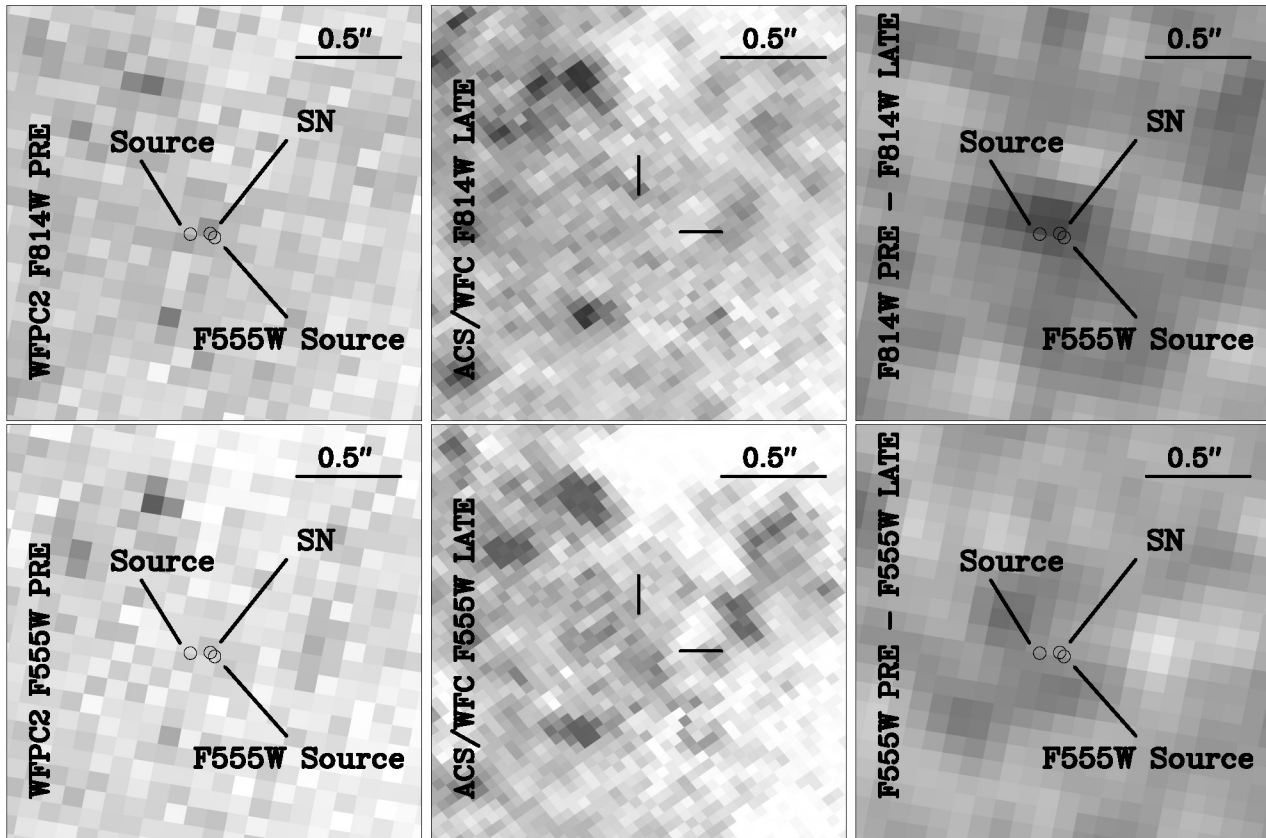


Figure 13. Pre-explosion and late-time HST images of the site of SN 2006my in the *F814W* (top row) and *F555W* (bottom row) bands. The transformed position of the SN and the positions of the sources detected in the pre-explosion *F555W* and *F814W* (labeled “source”) images are indicated by the circles.

the reddening. We consider the effects of foreground and host reddening to be due to Galactic-like dust (parameterised by $E(B - V)$; Cardelli et al. 1989). To constrain the effect of reddening due to dust expected to be found around RSGs, we consider the reddening laws for graphite or silicate dust (parameterised by the optical depth τ_v), contained in spherical shells with ratios for the inner and outer radii of $R_{out}/R_{in} = 2$ or 10, following Kochanek et al. (2012). For each SN site we adopt models with metallicities appropriate for that site (see Table 1).

To provide an additional handle on the interstellar reddening towards each progenitor, we also consider the reddening towards the stars immediately surrounding the SN position. Due to the distances of the host galaxies, the surrounding stars, which are selected based on the condition that they are detected in all three of the late-time images for each SN, are expected to be luminous OB stars. For each of the stars, the parameters T_{eff} and $E(B - V)$ are derived with respect to the ATLAS9 models. We selected those models from the ATLAS9 grid that are consistent with supergiant surface gravities (Laidler et al. 2008)¹². Total reddenings are derived with respect to a Cardelli et al. (1989) $R_V = 3.1$ reddening law, appropriate for reddening and extinction due to interstellar dust. The SED fits were conducted with the BIX Nested Sampling package (as all stars, by selection, had three colour photometry), such that the Bayesian evidence could be used to exclude those stars with colours clearly inconsistent with OB stars. Furthermore, to consider

the SEDs of compact clusters we adopt the model spectra produced using the STARBUST99 code (Leitherer et al. 1999).

For stellar progenitors, we derive masses using our various luminosity estimates (depending on the type of dust and star) following the technique of Smartt et al. (2009). Smartt et al. use predicted luminosities for the end-phases of STARS stellar evolution models (Eldridge & Tout 2004) to derive initial masses for progenitors with luminosities constraints derived from the observations. For a given luminosity, the progenitor is considered to lie in the mass range bounded at one end by the most massive star to end core He burning at that luminosity, and at the other by the least massive star to proceed to model termination (the onset of core Ne burning) at that luminosity (see Smartt et al. 2009, and their Fig. 1). We use STARS models calculated at integer initial masses, with the appropriate metallicities, and interpolate to determine the luminosities at the end of core He burning and the beginning of core Ne burning. This scheme characterises possible RSG progenitors. We also note that, at lower masses, some stars will undergo second dredge-up, causing them to become Asymptotic Giant Branch (AGB) stars that are cooler but more luminous than the similar mass stars that die as RSGs. Based on the observed temperature range of RSGs, derived using MARCS spectra (Levesque et al. 2005), we use a temperature threshold of 3400K, above and below which we consider stars to be RSGs or AGB stars, respectively.

In deriving posterior probability density functions (pdfs) for the initial masses for the progenitors, we also consider the effect of prior information from the IMF. We apply a weighting factor to the posterior pdfs $\propto M^{-2.35}$ for a Salpeter (1955) IMF, to follow the

¹² http://www.stsci.edu/hst/HST_overview/documents/synphot/AppA.Catalogs4.html

weighting scheme applied by Smartt et al. (2009) for their analysis of the Type IIP SN progenitor population.

4.1 SN 1999ev

The presence of a source in the late-time images precludes the use of image subtraction techniques to further analyse the nature of the pre-explosion source. We note that the pre-explosion $F555W$ magnitude of the source at the SN position is of similar magnitude to the source in the late-time $F555W$ image. The difference between the pre-explosion and late-time photometry is not significant with a p-value of 0.71 (using a simple z -test). This lends support to the hypothesis that the source observed in the pre-explosion images at the SN position has been recovered in the late-time images, and that the original identification of the progenitor presented by Maund & Smartt (2005) is, at least partially, incorrect. We suggest three possible scenarios for the nature of the source at the SN position:

(i) The source at the SN position in the pre-explosion and late-time images is a host cluster that contained the now absent progenitor.

(ii) The source observed in the pre-explosion and late-time image is an unrelated star that is coincident with the line-of-sight to the SN. While the late-time observations do suggest a large, young stellar population hidden by the large dust sheet, the determination of the likelihood of a chance alignment is non-trivial. Given the astrometric coincidence $< 0.04''$, it is likely to be very low.

(iii) The source observed in the late-time images is an unresolved light echo, and the pre-explosion source has now disappeared. Given the observation of evolving light echoes around the position of the SN, and the obvious amount of dust in the vicinity of the SN, the apparent late-time brightness may be due to a light echo from dust immediately behind the SN. We find this scenario unlikely, as it requires the progenitor and light echo to have coincidentally similar brightness.

Given the nature of the late-time three-colour imaging it is not possible to unambiguously distinguish between the different scenarios. The late-time images were used to examine the consequences of the progenitor residing in a host cluster that was observed in the pre-explosion and late-time images. The shape of the source in the late-time images was measured using the *ISHAPE* package (Larsen 1999). In each filter band, *ISHAPE* returned a significantly better fit with a Moffat function over a delta function ($\chi^2(\text{Moffat})/\chi^2(\text{delta}) < 0.95$) and an effective radius $R_{eff} > 0.1 \times$ the Full Width at Half Maximum (Larsen 1999). The effective radius of the source was measured to be $0.99^{+0.3}_{-0.55}$, $1.82^{+0.56}_{-1.07}$ and $1.18^{+0.12}_{-0.57}$ pixels in the $F435W$, $F555W$ and $F814W$, respectively (with a pixel scale corresponding to 2.7pc px^{-1} at the distance of NGC 4274). The large error bars are symptomatic of the complexity of the region hosting the SN, in particular with the proximity of light echoes and the apparent faintness of the source. The *ISHAPE* analysis was also conducted on six nearby objects that were all found to be consistent with point-like, stellar sources - suggesting that *ISHAPE* does have the capability, under the conditions of the late-time images, to differentiate extended sources from point-like sources. To further explore the implications of a host cluster for the progenitor, the late-time *ACS* photometry was compared with *STARBURST99* models (Leitherer et al. 1999); and the results of this fit is shown as Figure 14. Given the three colour photometry, there are two allowed solutions: a moderately reddened older solution (40 – 100 Myr) implying $M_{ZAMS} < 9M_{\odot}$; and a heavily reddened younger solution

($< 10 \text{Myr}$) implying $M_{ZAMS} > 20M_{\odot}^{13}$. In addition, given the criterion presented by Bastian et al. (2005), that point-like objects with $M_V < -8.6$ are more likely to be clusters than individual bright stars, requires $E(B - V) \geq 0.76$ (assuming an $R_V = 3.1$ Galactic reddening law). In terms of shape, absolute brightness and colours, the late-time source is consistent with a cluster. Using the photometry of nearby point-like sources, a weighted-average reddening of $E(B - V) = 0.95 \pm 0.32$ was measured. The large error bar is consistent with both the poor photometric errors for each of the six nearby sources and the large scatter in reddenings in the sample. The reddenings towards these objects are significantly greater than expected for just pure foreground Galactic reddening ($E(B - V) = 0.2$) towards NGC 4274. This may reflect a complex dust distribution where some of the sources are in front of the dust sheet and others may be embedded. This suggests that there might be significant reddening towards the source at the SN position, however this is not conclusive.

If the late-time source is, in fact, a light echo, then the late-time images do not provide any further insight into the properties of the source in the pre-explosion images. Our inability to confirm the disappearance of the progenitor also means that the late-time images cannot be used to rule out the possibility that the object in the pre-explosion and late-time images is an unrelated object in the line-of-sight. High-resolution near-infrared observations, with the HST, could be used to probe the nature of the stellar population behind the dust sheet (to examine the density of objects along the line-of-sight) as well as provide further constraints on the nature of the source in late-time images and nature of the obscuring dust. The ambiguity of the nature of the object at the SN position in the pre-explosion and late-time images means that, although SN 1999ev may have had an identified progenitor of some kind, the previously derived progenitor properties are unreliable; even in the interpretation that the source is a cluster, the reliance on three-colour photometry leads to degeneracies in the reddening-age solutions that prohibit a precise initial mass estimate for the progenitor.

4.2 SN 2003gd

The photometry of 30 stars within $4''$ ($\sim 200 \text{pc}$) of the position of SN 2003gd was used to derive an average reddening towards the SN site of $E(B - V) = 0.14 \pm 0.04$ (see Figure 15). The amount of reddening is consistent with the reddening previously estimated from three colour photometry of the surrounding stars using early post-explosion *ACS HRC* images (Smartt et al. 2004) and from the colour evolution of the SN itself (Hendry et al. 2005).

Given the detection of the progenitor in pre-explosion observations in two filters, we consider the roles of three different types of reddening: 1) unconstrained reddening, with an interstellar reddening law; 2) an interstellar reddening component consistent with the observed reddening to the surrounding stars and an unconstrained degree of reddening arising from Graphite dust around the progenitor; and 3) the same as 2, except with Silicate dust. The corresponding regions of the parameter space and the Hertzsprung-Russell (HR) diagram, allowed by the pre-explosion observations in conjunction with half-solar metallicity MARCS SEDs, are presented on Fig. 16. Given the observed colour of the progenitor, regardless of the amount of reddening, we find $T_{eff} > 3500 \text{K}$ and the

¹³ We note that the *STARBURST99* code uses the Padova stellar evolution (Girardi et al. 2002) models, and the masses we report for the derived ages are from these models.

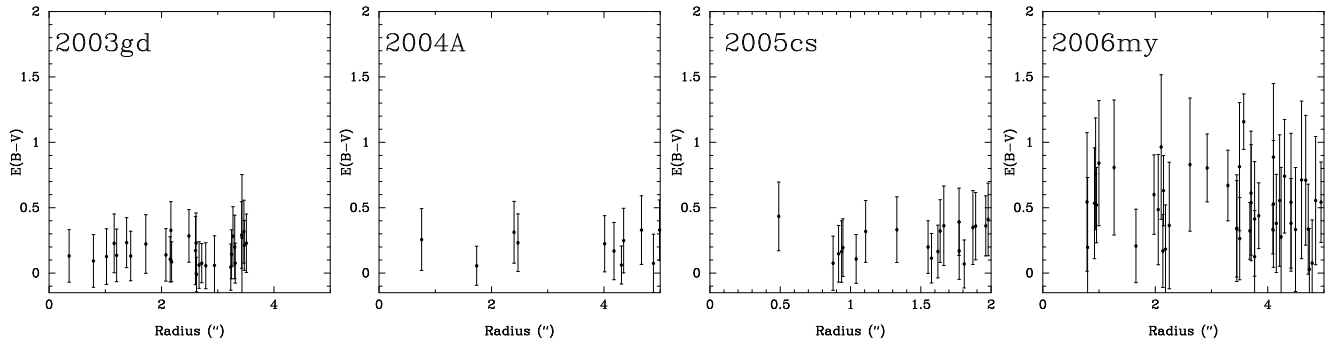


Figure 15. Reddenings for stars surrounding the sites of SNe 2003gd, 2004A, 2005cs and 2006my (as a function of distance from the SN positions).

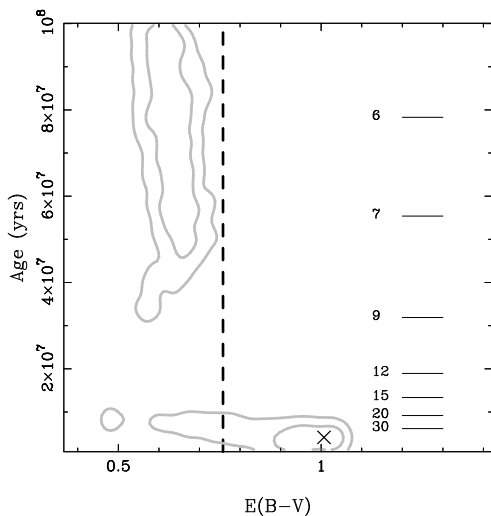


Figure 14. The posterior probability distribution for SED fits of the late-time photometry of the source at the position of SN 1999ev to cluster SED models produced using *STARBUST99*. The contours contain the 68% and 95% of the probability, while the most likely solution is indicated by the cross. The vertical dashed line corresponds to $E(B - V) = 0.76$; for $E(B - V) \geq 0.76$, the absolute magnitude of the source is $M_{F555W} < -8.6$. The horizontal lines indicate the lifetimes of stars with a given initial mass as predicted by the Padova stellar evolution code (Girardi et al. 2002).

radius of the progenitor constrained to be $200 < R < 400R_{\odot}$. The flatter nature of the graphite and silicate reddening laws, compared to the Cardelli et al. reddening law, leads to tighter luminosity constraints and a weaker dependence on the temperature/colour of the progenitor. The masses inferred for the progenitor are relatively insensitive to the choice of reddening law, with $M_{\text{init}} \sim 7 - 8 \pm 2.0M_{\odot}$.

Given the reddening derived towards SN 2003gd, we find that the SED of the object recovered at the SN position in the late-time images (A') is consistent with a black body with temperature $T \sim 9000\text{K}$, which is similar to the expected temperature for SNe at such late times (see e.g Otsuka et al. 2012).

4.3 SN 2004A

The three-colour photometry of 12 stars within $5.25''$ ($\approx 500\text{pc}$; see Fig. 15) of the position of SN2004A was used to derive a weighted average reddening towards the SN site of $E(B - V) = 0.16 \pm 0.06$. This is larger than the estimate made by Hendry et al. (2006) of

$E(B - V) = 0.06 \pm 0.03$, derived using three colour photometry from the post-explosion *ACS/WFC* images.

Due to the single *F814W* detection of the progenitor, and the upper *F606W* limit, an SED fit with > 1 parameter is underconstrained by the observations. Using particular prior assumptions, such as the reddening derived from surrounding stars, it is possible to probe the allowed likely parameter space. We conducted a two-parameter fit to MARCS SEDs, with half-solar metallicity, for temperature and a single reddening component (following a Cardelli et al. reddening law) with the reddening derived from surrounding stars as a prior. The resulting constraint in the temperature-reddening plane is shown on Figure 17. The low reddening and the strict *F606W* upper limit constrains the temperature of the progenitor to be lower than 3700K ; although this is sensitive to the reddening prior, such that higher reddenings may permit hotter progenitors. The corresponding region on the HR diagram is also shown on Figure 17. As the reddening is effectively fixed, the slope of the contours reflects the increasing bolometric correction for cooler stars. If the reddening inferred from the surrounding stars is, instead, a lower limit on the reddening towards the progenitor (due to an additional component of reddening due to circumstellar dust), then we can only derive a lower limit on the luminosity of the progenitor. The contours also include those stars in the initial mass range $5 - 7M_{\odot}$ that are expected, at this metallicity, to undergo second dredge up and become AGB stars.

4.4 SN 2005cs

The photometry, from the pre-explosion images, of 20 stars within $2''$ ($\sim 120\text{pc}$) of the position of SN 2005cs were used to determine a weighted average reddening towards the SN of $E(B - V) = 0.22 \pm 0.05$ (see Fig. 15).

In order to constrain the properties of the progenitors we utilised the *F814W* magnitude presented here, measured using image subtraction, and the revised detection thresholds for the pre-explosion *ACS F435W*, *F555W* and *F658N* images. Furthermore, we adopted the infrared detection limits for the progenitor reported for pre-explosion Gemini *NIRI JHK* images (Maund et al. 2005) and *NICMOS F110W*, *F160W F222M* images (Li et al. 2006a). As the *NICMOS* images are deeper, they form the principal constraint on the SED of the progenitor in the IR, however we include the Gemini *NIRI* limits in our calculation for completeness. We explored the same parameter space, for the same combinations of reddening components, as for the progenitor of SN 2003gd (see Section 4.2) and the results are presented on Fig. 18.

Similarly to the progenitor of SN 2003gd, the graphite and

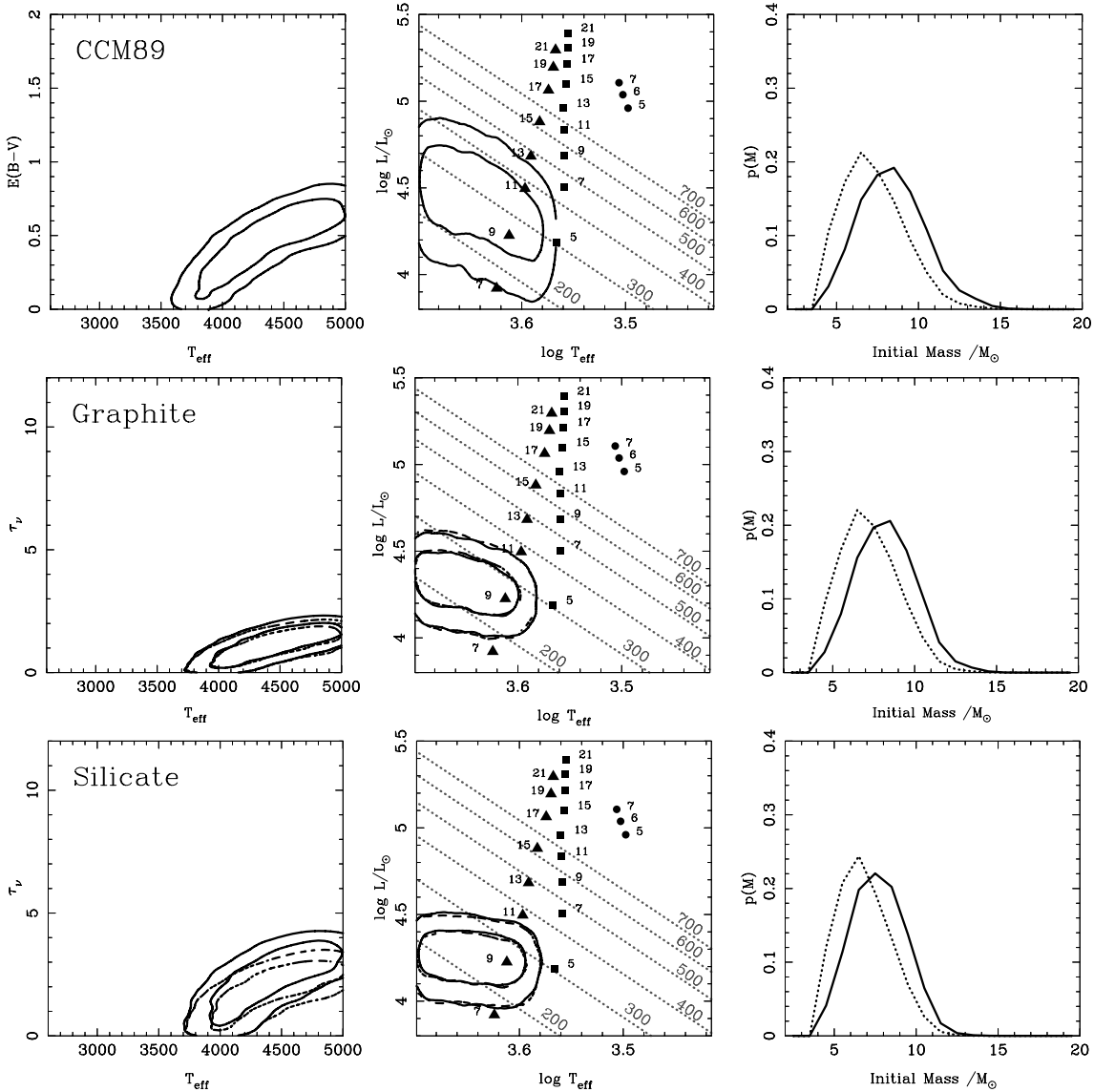


Figure 16. The parameters of the progenitor of SN 2003gd for different reddening components. In each panel the contours contain 68% and 95% of the total probability. *Top Row*, *Left*) The temperature and reddening of the progenitor assuming Galactic-like dust; *Centre*) the progenitor’s location on the HR diagram (also shown are the locations of stellar evolution models of given initial mass for the end of core He burning (\blacktriangle), the onset of Ne burning (\blacksquare) and the endpoints for those models that undergo second dredge-up (\bullet). Dotted grey lines indicate lines of constant progenitor radius.; and *Right*) the inferred initial mass probability density function with no weighting (solid line) and weighting according to the initial mass function (dotted line). *Middle Row*) The same as the top row, but for a Cardelli et al. (1989) reddening component of $E(B - V) = 0.14 \pm 0.04$, derived from the surrounding stars and an unconstrained reddening component for graphite dust around the progenitor (solid contours are for $R_{out}/R_{in} = 2$ and dotted contours are for $R_{out}/R_{in} = 10$). The mass probability density function are as for the top row, but only shown for the $R_{out}/R_{in} = 2$ solution. *Bottom Row*) The same as the middle row, but for silicate dust.

silicate reddening laws yield flatter contours of the HR diagram, making the dependence of the luminosity on the temperature less extreme. For each reddening type, there are two islands of preferred solutions: a cool, low reddened solution and a hotter, reddened solution; reflecting the severe constraints from non-detections in the infrared and in blue, respectively. The bimodal probability distribution in T_{eff} and $E(B - V)$ leads to a skewed mass probability density function for a Cardelli et al. reddening law extending to higher masses, although the peak of the distribution occurs at $\sim 10M_{\odot}$. For the graphite and silicate reddening laws, the unweighted mass probability density function is more symmetric and peaks around $\sim 11M_{\odot}$. The strict infrared limits exclude the possibility of the

progenitor being a massive AGB stars for all the reddening types (Eldridge et al. 2007).

4.5 SN 2006my

Previously Li et al. (2007) suggested that, apart from a Galactic reddening component, there was no evidence for a host reddening component in spectra of SN 2006my; this value was similarly used by progenitor studies conducted by Crockett et al. (2011) and Leonard et al. (2008). We utilised the HSTphot photometry of the post-explosion WFPC2 images of SN 2006my to study the reddening associated with the surrounding stellar population. We selected 46 good stars ($\chi^2 < 1.5$, $|\text{sharp}| < 0.3$) with complete three-colour

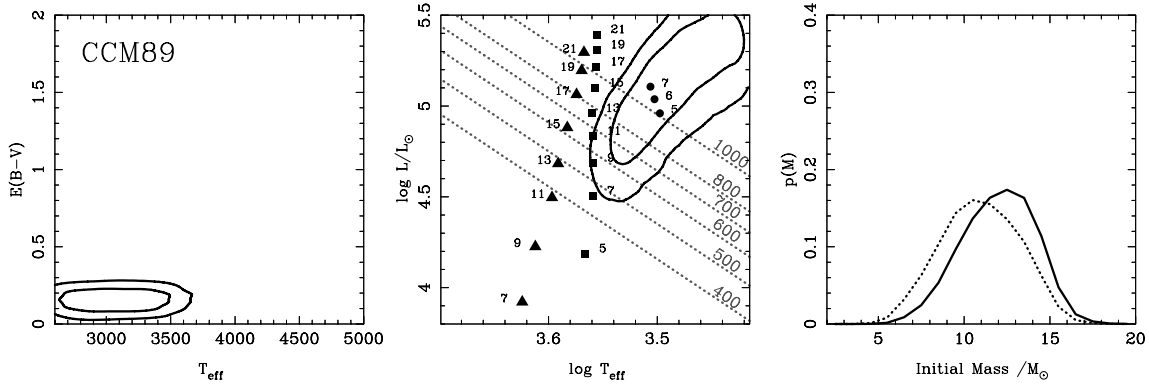


Figure 17. The same as Fig. 16 but for pre-explosion observations of the progenitor of SN 2004A, assuming only a Cardelli et al. reddening law with $E(B - V) = 0.06 \pm 0.03$ derived from surrounding stars.

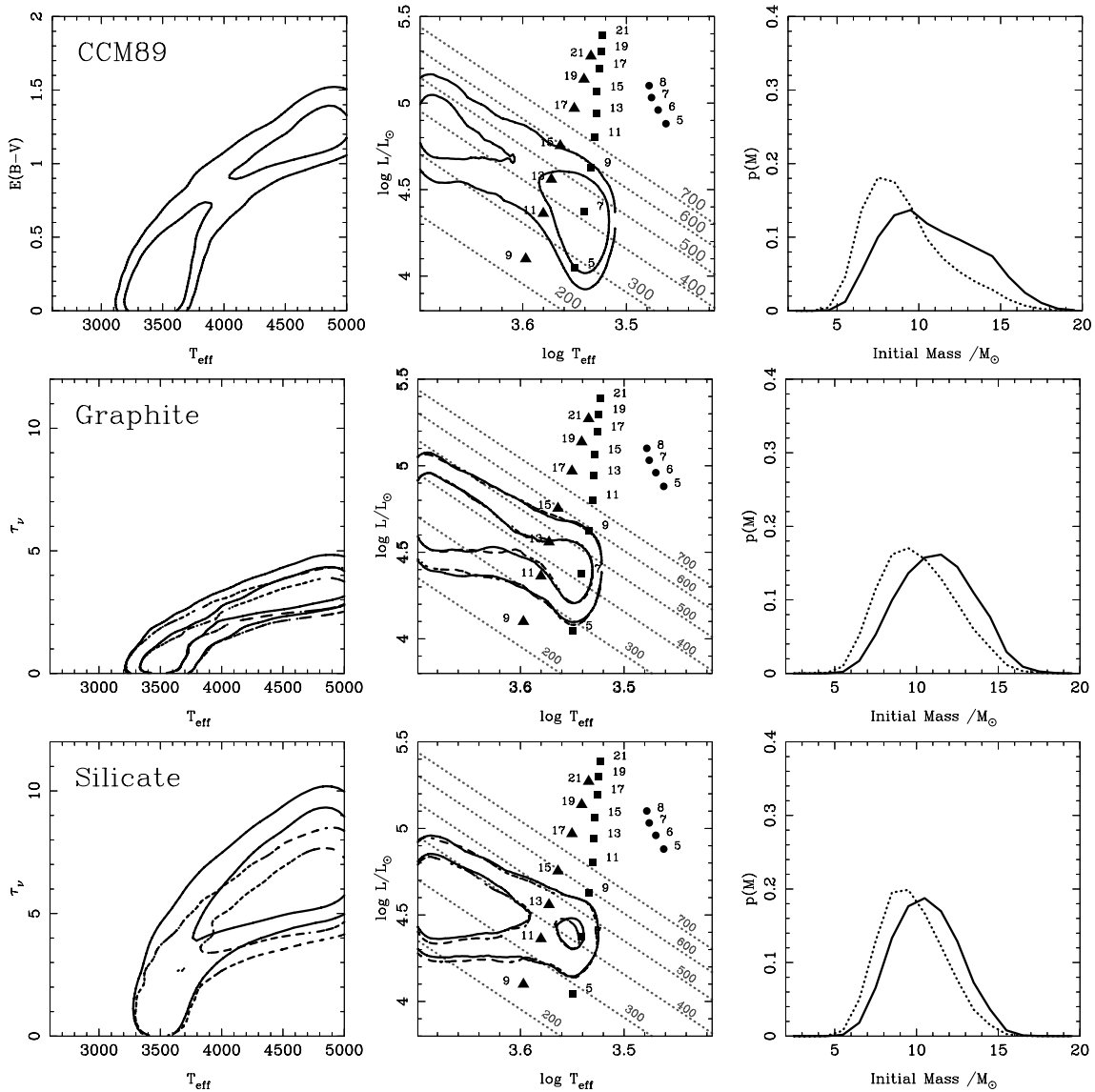


Figure 18. The same as Fig. 16, but for the pre-explosion observations of the progenitor of SN 2005cs.

photometry within $5''$ ($\sim 540\text{pc}$) of the SN. This photometry was compared with solar metallicity supergiant SEDs, to derive an average reddening towards SN 2006my of $E(B-V) = 0.49 \pm 0.25$ (see Fig. 15). The large scatter reflects the poor quality of the *WFPC2* photometry, as well as likely differences in the reddening between the individual stars. The relative colour constraint provided by the pre-explosion *F555W* limit and the *F814W* detection of the progenitor is insufficient to limit the temperature of the progenitor for temperatures below $< 4500\text{K}$. The allowed regions of the HR diagram, for the two reddening estimates, is shown on Figure 4.5. As for SN 2004A (see Section 4.3), the shape of the contours is dictated by the larger bolometric correction at cooler temperatures. The lack of an infrared detection or detection limit for the progenitor means that both the RSG and AGB solutions are allowed. The higher reddening inferred from the photometry of the surrounding stars implies higher luminosities for the progenitor, than for just Galactic foreground reddening, and leads to a higher initial mass (13.4 ± 2.8 vs. $9.8 \pm 1.7M_{\odot}$).

Given the apparent offset between the transformed SN position and the source recovered in the pre-explosion *F814W* image, we explored the possible causes for the apparent discrepancy. We note that all three previous studies, and our own results, agree that there is a significant offset between the transformed SN position and the pre-explosion *F814W* source. As noted by Leonard et al. (2008), in conjunction with Dolphin (2000b), the positional uncertainty for an isolated source with the brightness of the pre-explosion *F814W* source is ~ 0.4 pixels. We conducted Monte Carlo simulations, where the pre-explosion image was “resampled” under the assumption that the observed counts could be modelled as source and background flux (following a Poisson distribution) with a Gaussian readnoise contribution. Aperture photometry of these simulated images was conducted using DAOPhot, with the ofilter centring algorithm, to recover the position of the source (within a 5 pixel centring box). The result of these simulations is shown on Fig. 20 and the average position is $x = 410.5 \pm 0.5$, $y = 159.2 \pm 0.6$; offset from the SN position by 0.4 pixels. From the outcome of the Monte Carlo simulations we note three effects:

(i) The positional uncertainty is larger for faint sources and will be dependent on pixel noise statistics in the main pixel containing source flux and the surrounding pixels.

(ii) Given the subsampled nature of the PSF in *WFPC2* images, the uncertainty on the position of a source will also be dependent on the brightness of the immediately surrounding pixels; and, as evident from Fig. 20, the measured position may be skewed by the proximity of the true source position to a pixel edge.

(iii) The position derived is sensitive to the choice of centring algorithm utilised. Trials using the “centroid” centring algorithm in DAOPhot showed that positions were preferentially located at integer and half-integer pixel coordinates.

We conclude that, in addition to uncertainties associated with determining positions on *WFPC2* images for isolated sources, it is also important to consider the effects of nearby sources (within a few pixels) that may skew/bias the centring algorithm away from the true source position. From the Monte Carlo simulations, given the environment and pixel noise at the SN position, we estimate the uncertainty on the position of the pre-explosion *F814W* source may be $\sim 0.078''$. With such large uncertainties, the apparent offset between the SN and the pre-explosion source would be only $\sim 1\sigma$ given the offsets calculated by Crockett et al. (2011) and Leonard et al. (2008); however, we caution that our lower quality geometric transformation results in a 1.2σ offset.

5 DISCUSSION

A summary of the masses derived for the progenitors considered here is presented on Table 4. The biggest differences between our findings and those of Smartt et al. (2009) are for the progenitors of SNe 1999ev and 2006my. Our late-imaging shows that the nature of the source found at the SN position in pre-explosion observations of the site of SN 1999ev is, at best, uncertain; whilst, at worst, a misidentification of a host cluster or unrelated coincident star. As the nature of this source is not clarified in the late-time imaging, the progenitor of SN 1999ev should no longer be considered in progenitor population statistics. In the analysis presented by Smartt et al. (2009), the progenitor of SN 1999ev had the distinction of having the highest mass inferred for a detected Type IIP SN progenitor, and so set the maximum mass limit for stars to explode as RSGs and produce Type IIP SNe. With the removal of the SN 1999ev progenitor from the population statistics, the maximum mass limit will actually drop and make the “Red Supergiant Problem” even more severe. The late-time imaging of the site of SN 2006my has shown that the progenitor was detected in the pre-explosion observations, and the upper mass limit quoted by Smartt et al. should now be quoted as a detected progenitor with a corresponding mass estimate.

The mass estimates derived for the confirmed progenitors are generally higher (by $\sim 1M_{\odot}$) than those presented by Smartt et al.; in part, due to the slightly larger foreground and host reddenings we inferred towards the progenitors from the colours of the surrounding stars. In addition, for SN 2003gd and 2005cs we considered additional reddening components to the reddening from interstellar dust, in keeping with the expectation that there is dust local to progenitor that is not probed by the surrounding stars or the observations of the SNe. We also note that our uncertainties are smaller than those quoted by Smartt et al.: we considered the effects of uncertainties of the luminosity convolved with the flat probability distribution of the star having a mass in the range bounded by the maximum mass star to end core He-burning at that luminosity and the minimum mass star to begin Ne burning at that luminosity. The initial mass probability density functions are, apart from SN 2005cs, approximately symmetric and almost follow a normal distribution. We believe this is a fairer presentation of the initial masses for the progenitors and their uncertainties. The application of a weighting to the initial mass pdf, according to the IMF, has a small effect in shifting the pdf to slightly lower masses. Unlike Smartt et al. (2009), who used this weighting scheme to “truncate” their large uncertainties, we find that the effect of weighting on the relative width of the initial mass pdfs is minor.

The slight increase in the inferred progenitor mass does not help rectify the apparent discrepancy between these “evolutionary” masses and the progenitor masses derived from hydrodynamical models. Utrobin & Chugai (2008) found an initial mass for the progenitor of SN 2005cs of $18.2 \pm 1M_{\odot}$, which is at odds with the new masses derived here, regardless of the choice of reddening. As Utrobin & Chugai (2008) suggest, additional dust in a circumstellar shell could lower the apparent luminosity of the progenitor and decrease the mass inferred from pre-explosion observations. The nature of the pre-explosion observations of SN 2005cs, in particular the strict near-infrared upper limits, severely limits the amount of reddening that the progenitor might undergo. The constraints on the radius for the progenitor of SN 2005cs are also below the radius inferred by Utrobin & Chugai (2008) of $600 \pm 140R_{\odot}$, but not significantly discrepant.

It is clear from the analysis presented in Section 4, that the

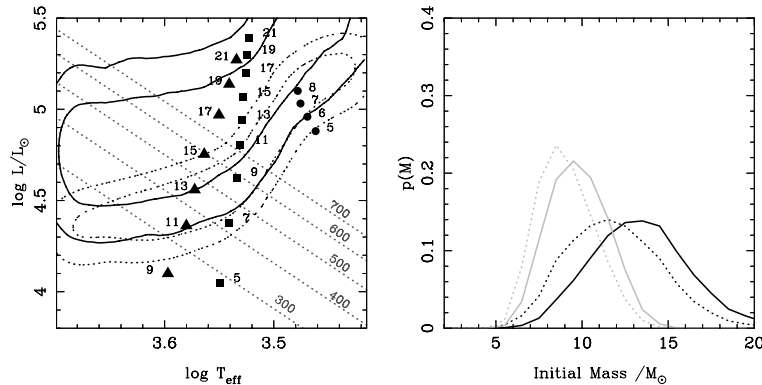


Figure 19. The parameters of the progenitor of SN 2006my. *Left*) The progenitor of SN 2006my on the HR diagram, assuming $E(B - V) = 0.49 \pm 0.25$ (solid contours) and $E(B - V) = 0.027$ (dotted contours). *Right*) The initial mass probability density functions for the progenitor of SN 2006my, given $E(B - V) = 0.49 \pm 0.25$ (heavy curves) and $E(B - V) = 0.027$ (grey curves).

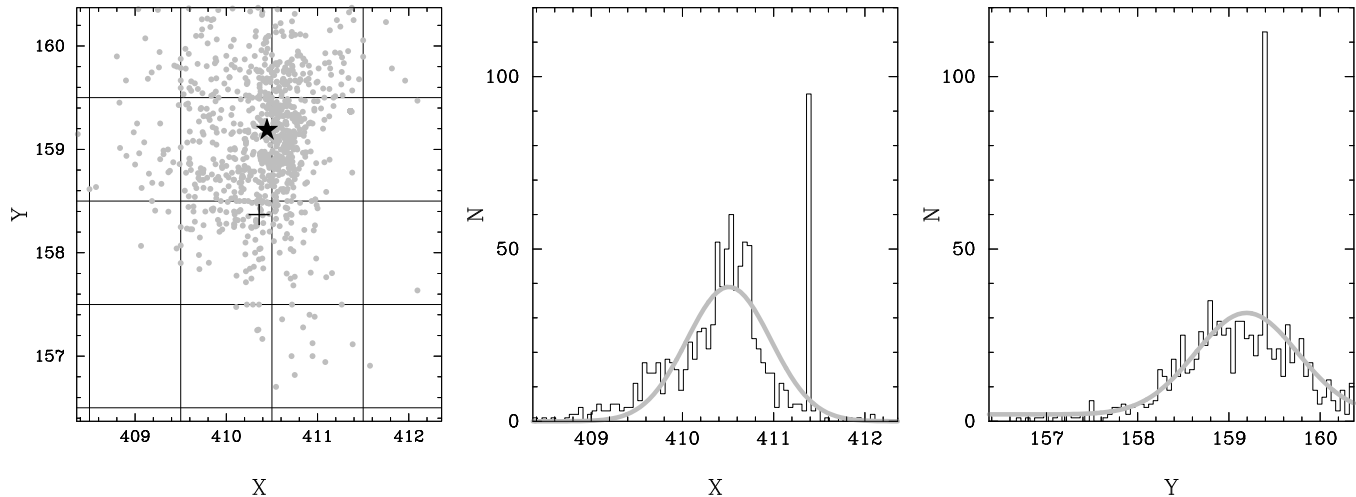


Figure 20. The results of position determinations for the pre-explosion source, using DAOPhot and the ofilter centring algorithm, for 1000 Monte Carlo simulations of the pre-explosion $F814W$ image of the site of SN 2006my. *Left*) The positions of the recovered sources in the coordinate frame of the original $WFPC2$ image (in the DAOPhot coordinate system). The position of the source recovered by HSTphot is indicated by the +, while the mean position derived from the Monte Carlo simulations is indicated by the \star ; *Centre and Right*) The position distributions in x and y coordinates for the recovered sources; the grey line indicates a Gaussian fit to the distributions.

available pre-explosion observations of a given SN progenitor dictates the degree of analysis that may be conducted. Given the presence of constraining optical and infrared upper limits, the possible effect of circumstellar reddening on the progenitor of SN 2005cs was evaluated despite having a detection in only one band. This demonstrates the importance for having good pre-explosion observations in the near-infrared for studying the cool progenitors of Type IIP SNe, even if the progenitor is not detected at those wavelengths. The two detections of the progenitor of SN 2003gd, at different wavelengths, enabled similar constraints for reddening due to circumstellar dust. Conversely, the analyses of SN 2004A and 2006my were limited by them having only a single detection and only loose constraint on the progenitor colour at a bluer wavelength.

Due to the lack of constraints on reddening due to circumstellar dust, the final derived masses for the progenitors of SNe 2004A and 2006my may represent, in actuality, lower mass limits. For this study, we have assumed the circumstellar dust follows the reddening laws proposed by Kochanek et al. (2012), for the case of the progenitor of SN 2012aw. Conversely, Van Dyk et al.

(2012) suggested a steeper reddening law, still following Cardelli et al., but with $R_V \approx 4.35$; leading to an overall higher extinction. The Kochanek et al. (2012) reddening law was determined using models of specific dust compositions, of either graphite or silicate dust, expected to be found around RSGs, whereas Van Dyk et al. (2012) estimated the change in reddening law based on observations of Galactic RSGs. For SN 2012aw (Fraser et al. 2012; Van Dyk et al. 2012), the progenitor was detected in four bands, and the degeneracies between reddening, reddening law and temperature could not be broken; suggesting the full determination of the parameters, independent of the assumptions of reddening laws, requires detections at > 4 wavelengths, such as for the progenitor of SN 2008bk (Mattila et al. 2008; Van Dyk et al. 2012).

Both Fraser et al. (2012) and Van Dyk et al. (2012) noted the large decrease in reddening determined for the pre-explosion source and for the subsequent SN; suggesting such large reddenings may affect all progenitors but not be apparent post-explosion. For their sample of RSGs, Davies et al. (2013) measure extinctions arising from circumstellar dust in the range $A_V = 0.0 - 1.0$. A further issue, that we have not explored, was suggested by Walmswell

& Eldridge (2012, and references therein) that the amount of dust in the circumstellar medium is related to the mass loss rate of the RSG and, ultimately, its bolometric luminosity.

A corresponding issue to the reddening problem is the temperature. We note that, for the progenitors with constraining pre-explosion observations, we find the allowed temperature range to be generally hotter than the predicted endpoints for the stellar evolution models, but are consistent with the recent reappraisal of RSG temperatures by Davies et al. (2013). The lower limit of the temperature scales for the progenitors of SNe 2003gd and 2005cs suggests that they have a spectral type no later than M0, which corresponds to the predicted positions for stars that have just finished core He-burning; the pre-explosion observations of SNe 2003gd and 2005cs suggest that the progenitors were not massive AGB stars (Eldridge et al. 2007; Siess 2007). It is only in the poorly constrained cases, for the progenitors of SNe 2004A and 2006my, that we cannot exclude cooler temperatures that might be associated with massive AGB stars. With limited observations in the optical (in particular the *B* and *V* bands), it is difficult to place limits on the maximum temperature of the progenitor, as hotter temperatures can always be accommodated with additional reddening. In the case of the progenitor of SN 2005cs, the requirement that the progenitor ended its life as an RSG has serious implications for the interpretation of the subsequent SN as a low luminosity “Electron-Capture” SN (Janka 2012).

Our late-time imaging campaign has shown that, for the case of SN 2003gd, the possibilities of recovering precise photometry of the progenitor through template subtraction may be undermined by rebrightening of the SN at late-times. In the case of SN 2003gd, the previous analysis of Maund & Smartt (2009) was fortuitous in that it managed to observe the SN before it rebrightened with a very strict brightness limit of the SN in the late-time *i'* image. Such rebrightening is not without precedent; Kotak et al. (2009) observed the optical lightcurve of SN 2004et to rebrighten (by ~ 1 mag in *V*) at optical and infrared wavelengths.

As noted in Section 4.5, the apparent discrepancy between the position of the progenitor of SN 2006my on the pre-explosion images and the transformed SN position does raise questions about how positional uncertainties are handled. Maund & Smartt (2005) determined the positional precision using the standard deviation of the four different centring methods available to DAOPHOT (centroid, ofilter, gauss and psf). It must be noted, however, that these centring techniques are not providing *independent* estimates of an object’s location. In the future, it may be preferable to choose a single centering technique, and consider the role of Poisson noise (both object and background) and read out noise in each pixel on the determination of an object’s position. Furthermore, tests using the centroiding routines in both the DAOPHOT and SAO image DS9 packages has shown that, in the case of isolated objects in subsampled images, centroiding can be a relatively blunt tool (providing default positions located in the centre of pixels). In considering flux deficits using image subtraction techniques, rather than appealing to astrometric coincidence, we have shown that confirmation of a star as being the actual progenitor requires observing it to have disappeared.

6 CONCLUSIONS

We have presented late-time imaging of the sites of five Type IIP SNe with pre-explosion HST images, in which progenitor candidates were detected. In three of the cases (2003gd, 2004A and

2005cs), our previous identifications have been confirmed and we find initial masses for these stars in the range $6 - 14M_{\odot}$. The pre-explosion observations of SNe 2003gd and 2005cs are sufficient to place constraints on the progenitor mass that are relatively insensitive to the amount and type of dust around these progenitors. Given the similarities in brightness between the pre-explosion and late-time sources detected at the position of SN 1999ev, we conclude the progenitor identification for this SN is unsafe and suggest the pre-explosion source may be a reddened host cluster; although the three-colour late-time imaging is insufficient to place a tight constraint on the age or reddening of a such cluster. The analysis of the pre-explosion and late-time observations of the site of SN 2006my have revealed that the source previously thought to be significantly offset from the SN position has disappeared. The astrometric coincidence of the residual in the difference image with the transformed SN position suggests it was the progenitor object.

Far from providing just simple confirmation of a progenitor’s identity (through its disappearance), our analysis shows late-time imaging is crucial for conducting a deeper and more precise analysis of the properties of a progenitor than is afforded by fortuitous pre-explosion observations alone. The power of the application of late-time imaging, for studying progenitors, is demonstrated by the significantly deeper detection limits that may be achieved by using artificial star tests in conjunction with image subtraction techniques.

ACKNOWLEDGEMENTS

Based on observations made with the NASA/ESA Hubble Space Telescope, which is operated by the Association of Universities for Research in Astronomy, Inc., under NASA contract NAS 5-26555. These observations are associated with program GO-11675. The research of JRM is funded through a Royal Society University Research Fellowship. We thank Stephen Smartt and Steen Hansen for their useful comments.

References

- Alard C., 2000, *A&AS*, 144, 363
- Alard C., Lupton R. H., 1998, *ApJ*, 503, 325
- Annibali F., Aloisi A., Mack J., Tosi M., van der Marel R. P., Angeretti L., Leitherer C., Sirianni M., 2008, *AJ*, 135, 1900
- Bastian N., Gieles M., Efremov Y. N., Lamers H. J. G. L. M., 2005, *A&A*, 443, 79
- Cardelli J. A., Clayton G. C., Mathis J. S., 1989, *ApJ*, 345, 245
- Castelli F., Kurucz R. L., 2004, *ArXiv Astrophysics e-prints*
- Chiaberge M., Lim P. L., Kozhurina-Platais V., Sirianni M., Mack J., 2009, Technical report, Updated CTE photometric correction for WFC and HRC. STScI
- Crockett R. M., Smartt S. J., Pastorello A., Eldridge J. J., Stephens A. W., Maund J. R., Mattila S., 2011, *MNRAS*, 410, 2767
- Davies B., Kudritzki R.-P., Plez B., Trager S., Lancon A., Gazak Z., Bergemann M., Evans C., Chiavassa A., 2013, *ArXiv e-prints*
- Dolphin A. E., 2000a, *PASP*, 112, 1397
- Dolphin A. E., 2000b, *PASP*, 112, 1383
- Drilling J. S., Landolt A. U., 2000, in Cox A. N., ed., *Allen’s Astrophysical Quantities*, 4 edn, AIP, New York
- Eldridge J. J., Mattila S., Smartt S. J., 2007, *MNRAS*, 376, L52
- Eldridge J. J., Tout C. A., 2004, *MNRAS*, 353, 87
- Evans R., McNaught R. H., 2003, *IAUC*, 8150, 2

Table 4. Final results for the progenitors of SNe 1999ev, 2003gd, 2004A, 2005cs and 2006my, for different reddenings due to instellar dust (CCM99) and circumstellar dust reddening laws (CSM Graphite and CSM Silicate).

SN	CCM89		CSM Graphite		CSM Silicate	
	w/ IMF	w/o IMF	w/IMF	w/o IMF	w/ IMF	w/o IMF
1999ev	Likely cluster	
2003gd	7.3 ± 1.9	8.4 ± 2.0	7.3 ± 1.8	8.2 ± 1.8	6.9 ± 1.6	7.7 ± 1.6
2004A	10.9 ± 2.3	12.0 ± 2.1
2005cs	7.9 ^{+2.6a} _{-1.6}	9.5 ^{+3.4a} _{-2.2}	10.1 ± 2.2	11.2 ± 2.2	9.7 ± 1.9	10.6 ± 1.9
2006my ^b	9.1 ± 1.7	9.8 ± 1.7
2006my ^c	11.9 ± 2.7	13.4 ± 2.8

^a The values corresponding the mode and 68% probability intervals.

^b Assuming foreground reddening $E(B - V) = 0.027$.

^c Assuming $E(B - V) = 0.49 ± 0.25$.

Fraser M., Maund J. R., Smartt S. J., Botticella M.-T., Dall’Ora M., Inserra C., et al. 2012, ArXiv e-prints

Garnavich P., Jha S., Kirshner R., Challis P., 1999, IAUC, 7306, 1

Girardi L., Bertelli G., Bressan A., Chiosi C., Groenewegen M. A. T., Marigo P., Salasnich B., Weiss A., 2002, A&A, 391, 195

Gustafsson B., Edvardsson B., Eriksson K., Jørgensen U. G., Nordlund Å., Plez B., 2008, A&A, 486, 951

Hendry M. A., Smartt S. J., Crockett R. M., Maund J. R., Gal-Yam A., Moon D., Cenko S. B., Fox D. W., Kudritzki R. P., Bann C. R., Østensen R., 2006, MNRAS, 369, 1303

Hendry M. A., Smartt S. J., Maund J. R., Pastorello A., Zampieri L., Benetti S., Turatto M., et al. 2005, MNRAS, 359, 906

Holtzman J. A., Hester J. J., Casertano S., et al. 1995, PASP, 107, 156

Hurst G. M., Boles T., Armstrong M., Schwartz M., 1999, IAUC, 7306, 1

Janka H.-T., 2012, Annual Review of Nuclear and Particle Science, 62, 407

Kawakita H., Kinugasa K., Ayani K., Yamaoka H., 2004, IAUC, 8266, 2

Kloehr W., Muendlein R., Li W., Yamaoka H., Itagaki K., 2005, IAUC, 8553, 1

Kochanek C. S., Khan R., Dai X., 2012, ApJ, 759, 20

Kotak R., Meikle W. P. S., Farrah D., Gerardy C. L., Foley R. J., Van Dyk S. D., Fransson C., Lundqvist P., Sollerman J., Fesen R., Filippenko A. V., Mattila S., Silverman J. M., Andersen A. C., Höflich P. A., Pozzo M., Wheeler J. C., 2009, ApJ, 704, 306

Kotak R., Meikle W. P. S., Smartt S. J., Bann C., 2003, IAUC, 8152, 1

Laidler V., Boffi F., Barlow T., Brown T., Friedman S., Jester S., Maiz Apellaniz J., Proffitt C., 2008, Synphot Data Users Guide. "STScI", "Baltimore"

Larsen S. S., 1999, A&AS, 139, 393

Leitherer C., Schaerer D., Goldader J. D., González Delgado R. M., Robert C., Kune D. F., de Mello D. F., Devost D., Heckman T. M., 1999, ApJS, 123, 3

Leonard D. C., Gal-Yam A., Fox D. B., Cameron P. B., Johansson E. M., Kraus A. L., Mignant D. L., van Dam M. A., 2008, PASP, 120, 1259

Levesque E. M., Massey P., Olsen K. A. G., Plez B., Josselin E., Maeder A., Meynet G., 2005, ApJ, 628, 973

Li W., Van Dyk S. D., Filippenko A. V., Cuillandre J.-C., Jha S., Bloom J. S., Riess A. G., Livio M., 2006a, ApJ, 641, 1060

Li W., Van Dyk S. D., Filippenko A. V., Cuillandre J.-C., Jha S., Bloom J. S., Riess A. G., Livio M., 2006b, ApJ, 641, 1060

Li W., Wang X., Van Dyk S. D., Cuillandre J.-C., Foley R. J., Filippenko A. V., 2007, ApJ, 661, 1013

Mattila S., Smartt S. J., Eldridge J. J., Maund J. R., Crockett R. M., Danziger I. J., 2008, ApJL, 688, L91

Maund J. R., Fraser M., Ergon M., Pastorello A., Smartt S. J., Sollerman J., Benetti S., Botticella M., Bufano F., Danziger I. J., Kotak R., Magill L., Stephens A. W., Valenti S., 2011, ArXiv e-prints

Maund J. R., Fraser M., Smartt S. J., Botticella M. T., Barbarino C., Childress M., Gal-Yam A., Inserra C., Pignata G., Reichart D., Schmidt B., Sollerman J., Taddia F., Tomasella L., Valenti S., Yaron O., 2013, ArXiv e-prints

Maund J. R., Smartt S. J., 2005, MNRAS, 360, 288

Maund J. R., Smartt S. J., 2009, Science, 324, 486

Maund J. R., Smartt S. J., Danziger I. J., 2005, MNRAS, 364, L33

Modjaz M., Kirshner R., Challis P., Hutchins R., 2005, IAUC, 8555, 1

Nakano S., Itagaki K., 2006, Central Bureau Electronic Telegrams, 727, 1

Nakano S., Itagaki K., Kushida R., Kushida Y., 2004, IAUC, 8265, 1

Otsuka M., Meixner M., Panagia N., Fabbri J., Barlow M. J., Clayton G. C., Gallagher J. S., Sugerman B. E. K., Wesson R., Andrews J. E., Ercolano B., Welch D., 2012, ApJ, 744, 26

Richmond M. W., Modjaz M., 2005, IAUC, 8555, 2

Salpeter E. E., 1955, ApJ, 121, 161

Schlafly E. F., Finkbeiner D. P., 2011, ApJ, 737, 103

Siess L., 2007, A&A, 476, 893

Sirianni M., Jee M. J., Benítez N., Blakeslee J. P., Martel A. R., Meurer G., Clampin M., De Marchi G., Ford H. C., Gilliland R., Hartig G. F., Illingworth G. D., Mack J., McCann W. J., 2005, PASP, 117, 1049

Smartt S. J., 2009, ARAA, 47, 63

Smartt S. J., Eldridge J. J., Crockett R. M., Maund J. R., 2009, MNRAS, 395, 1409

Smartt S. J., Maund J. R., Hendry M. A., Bann C. R., 2003, IAUC, 8152, 4

Smartt S. J., Maund J. R., Hendry M. A., Tout C. A., Gilmore G. F., Mattila S., Bann C. R., 2004, Science, 303, 499

Smith N., Li W., Filippenko A. V., Chornock R., 2011, MNRAS, 412, 1522

- Stanishev V., Nielsen T. B., 2006, Central Bureau Electronic Telegrams, 737, 1
- Utrobin V. P., Chugai N. N., 2008, A&A, 491, 507
- Van Dyk S. D., Cenko S. B., Poznanski D., Arcavi I., Gal-Yam A., Filippenko A. V., Silverio K., Stockton A., Cuillandre J.-C., Marcy G. W., Howard A. W., Isaacson H., 2012, ApJ, 756, 131
- Van Dyk S. D., Davidge T. J., Elias-Rosa N., Taubenberger S., Li W., Levesque E. M., Howerton S., Pignata G., Morrell N., Hamuy M., Filippenko A. V., 2012, AJ, 143, 19
- Van Dyk S. D., Li W., Cenko S. B., Kasliwal M. M., Horesh A., Ofek E. O., Kraus A. L., Silverman J. M., Arcavi I., Filippenko A. V., Gal-Yam A., Quimby R. M., Kulkarni S. R., Yaron O., Polishook D., 2011, ArXiv e-prints
- Van Dyk S. D., Li W., Filippenko A. V., 2003a, PASP, 115, 1
- Van Dyk S. D., Li W., Filippenko A. V., 2003b, PASP, 115, 1289
- Walmswell J. J., Eldridge J. J., 2012, MNRAS, 419, 2054